THE UNIVERSITY OF WARWICK

Library Declaration and Deposit Agreement

1. STUDENT DETAILS

Please complete the following:

Full name: Amar Suresh Parmar

University ID number: 0755499

2. THESIS DEPOSIT

2.1 I understand that under my registration at the University, I am required to deposit my thesis with the University in BOTH hard copy and in digital format. The digital version should normally be saved as a single pdf file.

2.2 The hard copy will be housed in the University Library. The digital version will be deposited in the University's Institutional Repository (WRAP). Unless otherwise indicated (see 2.3 below) this will be made openly accessible on the Internet and will be supplied to the British Library to be made available online via its Electronic Theses Online Service (EThOS) service.
[At present, theses submitted for a Master's degree by Research (MA, MSc, LLM, MS or MMedSci) are not being deposited in WRAP and not being made available via EthOS. This may change in future.]

2.3 In exceptional circumstances, the Chair of the Board of Graduate Studies may grant permission for an embargo to be placed on public access to the hard copy thesis for a limited period. It is also possible to apply separately for an embargo on the digital version. (Further information is available in the *Guide to Examinations for Higher Degrees by Research*.)

2.4 *If you are depositing a thesis for a Master's degree by Research, please complete section (a) below. For all other research degrees, please complete both sections (a) and (b) below:*

(a) Hard Copy

I hereby deposit a hard copy of my thesis in the University Library to be made publicly available to readers (please delete as appropriate) ~~EITHER~~ immediately ~~OR after an embargo period of ..... months/years as agreed by the Chair of the Board of Graduate Studies~~.

I agree that my thesis may be photocopied. YES / ~~NO~~ (*Please delete as appropriate*)

(b) Digital Copy

I hereby deposit a digital copy of my thesis to be held in WRAP and made available via EThOS.

Please choose one of the following options:

EITHER My thesis can be made publicly available online. YES / ~~NO~~ (*Please delete as appropriate*)

OR My thesis can be made publicly available only after…..[date] (Please give date)
YES / NO (*Please delete as appropriate*)

OR My full thesis cannot be made publicly available online but I am submitting a separately identified additional, abridged version that can be made available online.
YES / NO (*Please delete as appropriate*)

OR My thesis cannot be made publicly available online. YES / NO (*Please delete as appropriate*)

3. GRANTING OF NON-EXCLUSIVE RIGHTS

Whether I deposit my Work personally or through an assistant or other agent, I agree to the following:

Rights granted to the University of Warwick and the British Library and the user of the thesis through this agreement are non-exclusive. I retain all rights in the thesis in its present version or future versions. I agree that the institutional repository administrators and the British Library or their agents may, without changing content, digitise and migrate the thesis to any medium or format for the purpose of future preservation and accessibility.

4. DECLARATIONS

(a) I DECLARE THAT:

- I am the author and owner of the copyright in the thesis and/or I have the authority of the authors and owners of the copyright in the thesis to make this agreement. Reproduction of any part of this thesis for teaching or in academic or other forms of publication is subject to the normal limitations on the use of copyrighted materials and to the proper and full acknowledgement of its source.
- The digital version of the thesis I am supplying is the same version as the final, hard-bound copy submitted in completion of my degree, once any minor corrections have been completed.
- I have exercised reasonable care to ensure that the thesis is original, and does not to the best of my knowledge break any UK law or other Intellectual Property Right, or contain any confidential material.
- I understand that, through the medium of the Internet, files will be available to automated agents, and may be searched and copied by, for example, text mining and plagiarism detection software.

(b) IF I HAVE AGREED (in Section 2 above) TO MAKE MY THESIS PUBLICLY AVAILABLE DIGITALLY, I ALSO DECLARE THAT:

- I grant the University of Warwick and the British Library a licence to make available on the Internet the thesis in digitised format through the Institutional Repository and through the British Library via the EThOS service.
- If my thesis does include any substantial subsidiary material owned by third-party copyright holders, I have sought and obtained permission to include it in any version of my thesis available in digital format and that this permission encompasses the rights that I have granted to the University of Warwick and to the British Library.

5. LEGAL INFRINGEMENTS

I understand that neither the University of Warwick nor the British Library have any obligation to take legal action on behalf of myself, or other rights holders, in the event of infringement of intellectual property rights, breach of contract or of any other right, in the thesis.

Please sign this agreement and return it to the Graduate School Office when you submit your thesis.

Student's signature:  Date: 5th April 2013

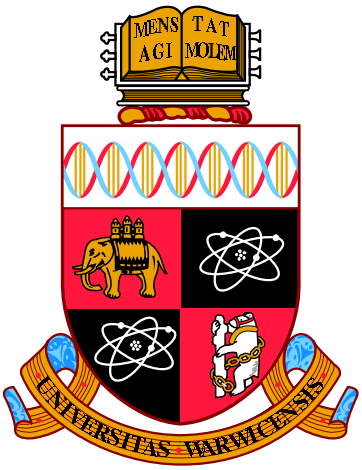

Numerical identification of fast structural growth in stratified turbulence

by

Amar S Parmar

Thesis

Submitted to The University of Warwick

for the degree of

Doctor of Philosophy

Mathematics Institute

March, 2012

THE UNIVERSITY OF WARWICK

Table of Contents

List of Figures

Acknowledgements

I would like to thank my supervisor, Prof. Robert Kerr, for his support, guidance and patience he has shown me during my time studying at Warwick University. I would also like to thank Colm Connaughton and Sergey Nazarenko for their interesting discussions over coffee.

A final thank you to the great friends I've made at Warwick and my family for their support and understanding.

Declaration

I wish to declare that this is my own work unless stated otherwise. I state that this thesis has not been submitted for a degree at another university.

Abstract

We investigate a type of instability observed in the presence of two counter rotating vortex columns in a highly stratified fluid, $Fr < 1$. This instability causes the vortex columns to be bent and stretched out in the horizontal direction eventually leading to discrete horizontal layers of vorticity. The instability is known as the zigzag instability and causes exponential growth in total enstrophy which stops once viscous dissipation becomes important. We find that two counter rotating vortex columns with localised perturbations applied parallel to the direction of propagation and offset from one another between the two columns is an initial profile that is highly unstable to the zigzag instability leading to exponential enstrophy growth faster than any prior numerical simulations have shown however is consistent in timing with a previous experimental result. We show that the zigzag instability that develops on these vortex columns provides a mechanism for energy (kinetic and potential) to cascade from large scales to small scales.

Notation and Parameters

Name	Notation
Froude Number	Fr
Richardson Number	Ri
Reynolds Number	Re
Brunt Väisälä Frequency	N
Density	ρ
Gravitational Force	$g\hat{\boldsymbol{z}}$
Pressure	p
Velocity	$\boldsymbol{u}$
Vorticity	$\boldsymbol{\zeta}$
Viscosity	ν
Diffusivity	κ
Potential Temperature	θ
Strain	S
Thermal Expansion Coefficient	α
Potential Vorticity	$\boldsymbol{\zeta} \cdot \nabla\theta$
Potential Energy	$\frac{1}{2}\theta^2$
Kinetic Energy	$\frac{1}{2}\boldsymbol{u}^2$
Enstrophy	Z
Vortex Stretching	$\boldsymbol{\zeta} S \boldsymbol{\zeta}$
Baroclinic Term	$\alpha g \hat{\boldsymbol{z}} \boldsymbol{\zeta} \times \nabla\theta$

Chapter 1

Introduction

The nature of turbulent flow means it can potentially act on a huge range of scales, from the very small, through the medium scales that influence the human environment to the vast length scales of planets, solar systems and galaxies. These turbulent flows exist in even the simplest of everyday occurrences, such as the water passing down a plug hole, the movement of air behind a travelling aeroplane and perhaps one of the most important aspects of daily human life, the weather. The on set of turbulence is a complex topic, not least because its characteristics are often defined by a variety of parameters. As an example, the turbulent structures in the Earth's atmosphere develop and evolve from influences such as the rotation of the planet, heating of the upper layer of the atmosphere by our sun, heating from the surface of the Earth itself, the radius of Earth, its gravitational strength and the fact that that horizontal length scale of the atmosphere is many times greater than the vertical length scale. These though are yet only a few examples of the possible factors that shape the turbulence of Earth's atmosphere. However, they are more than sufficient to realise immediately that the turbulent structures in the atmosphere of Earth will not be precisely the same on any other of our solar systems planets and perhaps even our galaxies.

Prior to the mathematical study of fluid dynamics, it was the work of Leonardo

da Vinci in the 15^{th} century that first made record of the various structures and formations within a turbulent flow. The study of turbulence through the use of mathematics was made possible after the development of calculus in the 17^{th} century independently by Newton and Leibnitz which Euler (1757) used to derive an equation for fluid motion based on the principle of momentum conservation

$$\frac{\partial \boldsymbol{u}}{\partial t} + (\boldsymbol{u} \cdot \nabla)\, \boldsymbol{u} = \frac{-1}{\rho} \nabla p \tag{1.1}$$

Though Euler's equation is certainly of mathematical interest, physically its interpretation of fluid motion is limited. One of its primary flaws is the lack of modelling of the interaction between particles which converts kinetic energy to dissipated heat. Euler's model was improved upon, to take account of energy transitions, by Navier and Stokes independently to give the famous Navier-Stokes equation

$$\frac{\partial \boldsymbol{u}}{\partial t} + (\boldsymbol{u} \cdot \nabla)\, \boldsymbol{u} = \frac{-1}{\rho} \nabla p + \nu \nabla^2 \boldsymbol{u} + \boldsymbol{f} \tag{1.2}$$

Coupled with this Navier-Stokes equation, the assumption that the fluid is incompressible,

$$\nabla \cdot \boldsymbol{u} = 0 \tag{1.3}$$

give the fundamental equations that, to this day, many fluid dynamicists study. The addition of the term related to viscosity, $\nu \nabla^2 \boldsymbol{u}$, gives rise to the most significant difference between the Navier-Stokes and Euler's equation, that of irreversibility. Given a fluid state at some time (greater than zero) one is able to trace back the motions of the particles to derive the initial state of the fluid (at time zero) if the flow is modelled by Euler's equation. On the other hand, due to the various transfers of energy during molecule collision, which is accounted for in the Navier-Stokes equation, one is unable to conclusively determine the initial state if the flow evolves according to Navier-Stokes dynamics. However, with the addition of the viscous

term, Kolomogorov (1941) was able to show one of the few analytical results of the Navier-Stokes equations relating to energy dissipation.

1.1 Kolmogorov 1941

Turbulent flow involves various scales of motion; large scales that are usually determined by forces and boundaries and small scale motions that obtain their energy from the larger scales. The flow of energy from large scales to small scales proceeds as large scale structures break down into smaller scales which then intern break up to give even smaller scale structures. This process of energy transfer and structure break down continues until the structures become so small that the viscous effects of the fluid dominate over the motion of the structure and then all their energy is dissipated through viscous diffusion.

We define these organised motions of the fluid as eddies. Let the velocity field of a fluid with these so called eddies be defined by the Fourier series [4]

$$\boldsymbol{u}(\boldsymbol{x}) = \sum \tilde{\boldsymbol{u}}(k)\, e^{\mathrm{i}k\boldsymbol{x}}$$

and where $\tilde{\boldsymbol{u}}(k)$ can be associated with eddies of the size k^{-1}. If we consider a homogeneous flow which has energy spectrum $E(k)$, and a dissipation spectrum given by $2Re^{-1}k^2E(k)$ then for large Reynolds number, Re, k must also be large for the dissipation spectrum to be significant. Then, the question is, what happens in the range between when the energy spectrum is significant and when the dissipation spectrum is significant? Assuming that $\max(E(k))$ occurs when $k = k_1$ and $\max(2Re^{-1}k^2E(k))$ occurs when $k = k_2$ (clearly $k_1 \ll k_2$) we call the range of wavenumbers between k_1 and k_2 the *inertial range*[4]. It seems conceivable that in this inertial range, after the energy spectrum is large and before the energy dissipates away, that energy passes through it on the way to be dissipated. If this is indeed

true, then we could postulate that the energy, $E(k)$, in this range would depend on the wavenumber, k, and the rate per unit at which energy is being transported through the inertial range, ε. That is [5]

$$E(k) \propto \varepsilon^{\beta} k^{\gamma}$$

Mathematically, we define ε as the averaged sum of squared quantities (hence $\varepsilon \geq 0$),

$$\varepsilon = \nu \left\langle \left(\frac{\partial u_i}{\partial x_j} + \frac{\partial u_j}{\partial x_i} \right) \left(\frac{\partial u_i}{\partial x_j} + \frac{\partial u_j}{\partial x_i} \right) \right\rangle$$

using the standard Einstein summation convention. Dimensionally, the units of; $E(k)$ is $\frac{L^3}{T^2}$, ε is $\frac{U^2}{T}$ or equivalently $\frac{L^2}{T^3}$ and k is $\frac{1}{L}$. Then, dimensionally analysis yields the only possible solution for β and γ as,

$$\beta = \frac{2}{3}\,, \quad \gamma = 2\beta - 3 = \frac{-5}{3}$$

so finally, we have

$$E(k) = C\varepsilon^{2/3} k^{-5/3} \tag{1.4}$$

for some constant, C.

1.2 Atmospheric Energy Spectrum

The motions within fluids span a wide range of scales, from the large, which in 3D turbulence energy is supplied, to the small scales at which 3D turbulence predicts that energy will be dissipated. These motions and interactions of the fluid passes energy along the scales within the fluid, a process known as an energy cascade. In a fully 3D turbulent system the proposed energy cascade moves energy from large scales to small scales at which it is dissipated, this is known as a forward energy cascade. Conversely, an inverse energy cascade, is characterised by small scale struc-

tures transferring energy into the large scale structures by amalgamating themselves into these larger structures, this form of energy cascade is typical of 2D turbulence. Regarding the atmosphere, it would seem that the conclusions based on 2D turbulence would hold since the vertical length scale of the atmosphere is much less than that of the horizontal length scale, and thus an inverse energy cascade would be expected. However, this has been shown not to be the case and in fact the energy cascade is a forward one as predicted by fully developed 3D turbulence. This is somewhat puzzling, the physical relationship between the vertical and horizontal length scales in the atmosphere do not support the idea of fully developed 3D turbulence but nor does the energy spectrum support the idea of 2D turbulence. Perhaps a mechanism exists to transfer energy downscale similar in concept to 3D turbulence but different in its mechanism?

The Kolmogorov prediction of the energy spectrum, (1.4) - $k^{-5/3}$, is something that has been observed experimentally in the atmosphere. In 1985 Nastrom and Gage [1] published results based on data that was gathered from various aircraft flights. In the data they obtained, for length scales of 10^3km down to 10km, Nastrom and Gage where able to clearly identify a $k^{-5/3}$ regime as predicted by Kolmogorov; this result is reproduced in Fig. 1.1. This $k^{-5/3}$ observed experimentally in the mesoscales has also been verified by Cho and Lindborg (2001, [6]) again using data collated from several thousand aircraft flights over a period of three years. From this data, Cho and Lindborg computed the third-order structure function [6], the sign of which describes the direction of energy cascade. A positive third-order structure function would imply an inverse energy cascade from small scales to large scales and a negative third-order structure function the opposite. The third order structure function is a two point velocity correlation measure defined as [7],

$$S_3^{(\eta)} = \left\langle \left| \boldsymbol{u}\left(\boldsymbol{x}+\eta, t\right) - \boldsymbol{u}\left(\boldsymbol{x}, t\right) \right|^3 \right\rangle$$

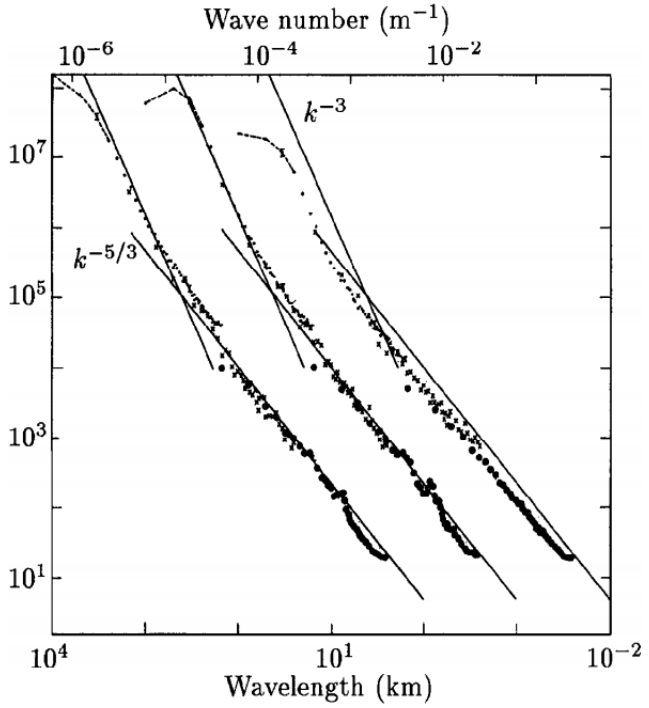

Figure 1.1: Variance power spectra of wind and potential temperature near the tropopause from GASP aircraft data. Reproduced from Nastrom and Gage [1, Fig. 3].

where $\langle \cdot \rangle$ is a usual space-time average metric. Through statistical averaging of homogeneous isotropic flow, Kolmogorov (1941) obtained the relationship for S_3 in the case of an ideal forward energy cascade in three dimensions as,

$$S_3(\eta) = \frac{-4}{3}\varepsilon\eta$$

Since ε is the sum of squared average quantities it is greater than or equal to zero, hence Kolmogorov has shown that a negatively signed third order structure function implies the existence of a forward energy cascade in three dimensions.

Cho and Lindborg (2001, [6]) found that in the mesoscales of the lower atmosphere the sign of the structure function indicated a downscale cascade of energy. Previous theories had suggested that the energy cascade would be an inverse one based on the arguments of two-dimensional turbulence [8], however given support for a forward cascade from the structure function and further evidence provided in

direct numerical simulation by Riley and deBruynKops (2003, [9]) the argument for a cascade of energy from large scales to small scales is compelling. The simulations performed by Riley and deBruynKops (2003, [9]) of strongly stratified turbulence show not only an energy spectrum close to $k^{-5/3}$ but also that this spectrum is a forward cascade to smaller scales [9, Fig. 10]. The fact that energy spectrum has a $k^{-5/3}$ law, just as one observes in three dimensional isotropic turbulence is surprising [10] given that in the mesoscales, horizontal length scales are typically much larger than those of the vertical and so dynamics of fully three dimensional turbulence cannot be invoked.

The scenario in which we sit is that the $k^{-5/3}$ energy spectrum of the mesoscale can not be explained by the same arguments as fully three dimensional turbulence since the physical settings do not agree, nor can it be explained by two dimensional turbulence arguments since the directions of the energy cascades do not match. Hence there must be other explanation which will allow for energy to cascade to small scales in the mesoscales. Proposed mechanisms for this have included storm generation, Kelvin-Helmholtz instabilities and dynamics of stratified turbulence. In highly stratified fluids an instability, known as the zigzag instability (Chapter 3), has been observed [2, 11, 12] and is proposed as a method for energy to cascade to small scales.

Further motivation to understand the dynamics of stratified turbulence in the mesoscales and the corresponding energies, arises in current numerical weather predictions models.

1.3 Numerical Weather Prediction Models

The European Centre for Medium-Range Weather Forecasts (ECMWF) aim to provide operational medium- and extended-range weather forecasts using an ensemble prediction system (`http://www.ecmwf.int`). When these models are run in forecast

mode, it is known that they do not achieve the $k^{-5/3}$ spectrum in the mesoscales [13]. A possible explanation for this could be due to the truncation error [13] in computing the advection scheme (an example of which being semi-Lagrangian) resulting in an overall smoothing effect. Shutts (2005) details this argument to propose injection of energy back at the grid scale to compensate for the increased diffusion using a stochastic forcing approach.

The artificial smoothing caused by the truncation error, could conceivably cause any instabilities and discontinuities to be smoothed out before they have had a chance to grow which, in the case that they provide a route for energy dissipation, would impact the energy spectrum observed in these models. If one is able to show that it is possible for small scale structures to provide a route for energy to be dissipated, then in a practical sense modifications could be made to current numerical weather prediction models in order to compensate for this loss of energy pathway.

1.4 Main Results of Thesis

In this thesis we shall detail a new set of initial vortex profiles that become unstable to the zigzag instability faster than any prior numerical simulations have previously and thus will closer match the experimental results obtained by Billant and Chomaz (2000, [2]). Prior numerical calculations have concentrated on perturbing the initial velocity field of the simulation, however the consequence of this is that this perturbation will act symmetrically on a pair of vortex columns within the fluid. We propose a new approach of perturbing directly the vorticity field of each vortex column independently of each other, allowing for an initial perturbed set-up which has the perturbations to each vortex column vertically offset from the perturbation on the other column. We will see that it is precisely this new approach that will allow for the onset and development of the zigzag instability faster than that seen

previously.

Given this new family of perturbations we will consider the cascades of energy and show evidence of energy cascade from large scales to small scales, a forward energy cascade. Based upon this evidence we postulate that the lack of a numerically observed $k^{-5/3}$ energy spectrum in numerical weather prediction models could, in part, be explained by these types of models smoothing out small scale structures, such as the zigzag instability, which, if resolved fully, is able to provide an alternate route for energy to dissipate from large to small scales.

1.5 Thesis Structure

In Chapter 2 we will outline the equations that govern the fluid flow along with specific geophysical approximations. We will begin with the well known Navier Stokes equations and derive a set of equations under an assumption of small density and pressure differences, known as the Boussinesq approximation. Given these equations we will derive an alternate form based on vorticity rather than velocity. Finally we will give the equations that define change in enstrophy and kinetic energy.

In Chapter 3 we will describe the zigzag instability, including what characterises it, evidence in experimental works and previous study of it in direct numerical simulations.

Chapter 4 will detail a set of direct numerical simulations (DNS) performed. We will begin by replicating the DNS that has been done prior by Deloncle et al. (2008, [3]) and show matching isosurfaces of enstrophy and plots of total enstrophy evolution. We will then propose four new initial conditions that will be unstable to the zigzag instability and will identify one of these as being the most unstable to the instability. We show that this new more unstable initial condition has much faster growth in enstrophy, developing the zigzag instability much faster than prior DNS and in the same timescales as that of experimental studies [2]. We will consider the

enstrophy in its components in x, y and z as well as its components of stretching and barolinic production. Finally, we show the evolution of kinetic and potential energy in physical space and also their spectra and transfer spectra in Fourier space.

Finally, we draw conclusions based on the new DNS and highlight some topics that require further investigation.

Chapter 2

Governing Equations

2.1 Boussinesq Approximation

To derive the Boussinesq approximation of the Navier-Stokes equations begin with the full compressible Navier-Stokes equations

$$\frac{\partial \boldsymbol{u}}{\partial t} + (\boldsymbol{u} \cdot \nabla)\, \boldsymbol{u} = \frac{-1}{\rho} \nabla p + \nu \nabla^2 \boldsymbol{u} + g\hat{\boldsymbol{z}} \tag{2.1}$$

which quantities as defined in the preamble - 'Notation and Parameters.'

Now let us define some basic pressure and density profiles (determined by setting $\boldsymbol{u} = 0$ in (2.1)) as $\bar{p}\,(\boldsymbol{x})$ and $\bar{\rho}\,(\boldsymbol{x})$ [4]. Assume that the actual pressure and density fields are close to this previously defined basic state. That is,

$$\begin{aligned} p\,(\boldsymbol{x}, t) &= \bar{p}\,(\boldsymbol{x}) + p'\,(\boldsymbol{x}, t) \\ \rho\,(\boldsymbol{x}, t) &= \bar{\rho}\,(\boldsymbol{x}) + \rho'\,(\boldsymbol{x}, t) \end{aligned} \tag{2.2}$$

By 'close' we imply that, $|p'| \ll \bar{p}$ and $|\rho'| \ll \bar{\rho}$. By replacing (2.2) in to the Navier

Stokes equation, (2.1), we obtain

$$\begin{aligned}
\frac{\partial \boldsymbol{u}}{\partial t} + (\boldsymbol{u}\cdot\nabla)\,\boldsymbol{u} &= \frac{-1}{\bar{\rho}+\rho'}\nabla\left(\bar{p}+p'\right) + \nu\nabla^2\boldsymbol{u} + g\hat{\boldsymbol{z}} \\
\Rightarrow \frac{\partial \boldsymbol{u}}{\partial t} + (\boldsymbol{u}\cdot\nabla)\,\boldsymbol{u} &= \frac{-1}{\bar{\rho}+\rho'}\nabla\bar{p} + \frac{-1}{\bar{\rho}+\rho'}\nabla p' + \nu\nabla^2\boldsymbol{u} + g\hat{\boldsymbol{z}}
\end{aligned}$$

Since $\bar{\rho}g\hat{\boldsymbol{z}} = \nabla\bar{p}$ [4] then

$$\begin{aligned}
\frac{\partial \boldsymbol{u}}{\partial t} + (\boldsymbol{u}\cdot\nabla)\,\boldsymbol{u} &= \frac{-\bar{\rho}g\hat{\boldsymbol{z}}}{\bar{\rho}+\rho'} - \frac{1}{\bar{\rho}+\rho'}\nabla p' + \nu\nabla^2\boldsymbol{u} + g\hat{\boldsymbol{z}} \\
\Rightarrow \left(\bar{\rho}+\rho'\right)\left[\frac{\partial \boldsymbol{u}}{\partial t} + (\boldsymbol{u}\cdot\nabla)\,\boldsymbol{u}\right] &= -\bar{\rho}g\hat{\boldsymbol{z}} - \nabla p' + \left(\bar{\rho}+\rho'\right)\nu\nabla^2\boldsymbol{u} + \left(\bar{\rho}+\rho'\right)g\hat{\boldsymbol{z}} \\
\Rightarrow \left(1+\frac{\rho'}{\bar{\rho}}\right)\left[\frac{\partial \boldsymbol{u}}{\partial t} + (\boldsymbol{u}\cdot\nabla)\,\boldsymbol{u}\right] &= -g\hat{\boldsymbol{z}} - \frac{1}{\bar{\rho}}\nabla p' + \left(1+\frac{\rho'}{\bar{\rho}}\right)\nu\nabla^2\boldsymbol{u} + \left(1+\frac{\rho'}{\bar{\rho}}\right)g\hat{\boldsymbol{z}}
\end{aligned}$$

Now, since, $|\rho'| \ll \bar{\rho} \Rightarrow \frac{\rho'}{\bar{\rho}} \ll 1$ then we shall neglect these terms (although not those multiplied by $g\hat{\boldsymbol{z}}$ since $g\hat{\boldsymbol{z}} \sim O\left(\bar{\rho}\right)$).

$$\therefore \frac{\partial \boldsymbol{u}}{\partial t} + (\boldsymbol{u}\cdot\nabla)\,\boldsymbol{u} = -\frac{1}{\bar{\rho}}\nabla p' + \nu\nabla^2\boldsymbol{u} + \frac{\rho'}{\bar{\rho}}g\hat{\boldsymbol{z}}$$

If then, we define an average density level and call this average ρ_0 and further assume that the basic state density, $\bar{\rho}\left(\boldsymbol{x}\right)$, is close to ρ_0[1] then we have

$$\frac{\partial \boldsymbol{u}}{\partial t} + (\boldsymbol{u}\cdot\nabla)\,\boldsymbol{u} = -\frac{1}{\rho_0}\nabla p' + \nu\nabla^2\boldsymbol{u} + \frac{\rho'}{\rho_0}g\hat{\boldsymbol{z}} \tag{2.3}$$

With some change of notation; drop the prime from p, non-dimensionalise the viscosity by using the Reynolds number, Re, and rewrite $\frac{\rho' g}{\rho_0}$ as θ, the potential temperature (this is an ideal gas law [14]), we finally obtain the Navier Stokes equations

[1] This assumption is equivalent to assuming that the thickness of the layer is small with respect to the total depth

under the Boussinesq approximation,

$$\frac{\partial \boldsymbol{u}}{\partial t} + (\boldsymbol{u} \cdot \nabla)\, \boldsymbol{u} = -\frac{1}{\rho_0}\nabla p + \theta \hat{\boldsymbol{z}} + Re^{-1}\nabla^2 \boldsymbol{u} \tag{2.4}$$

$$\frac{\partial \theta}{\partial t} + (\boldsymbol{u} \cdot \nabla)\, \theta = \kappa \nabla^2 \theta \tag{2.5}$$

$$\nabla \cdot \boldsymbol{u} = 0 \tag{2.6}$$

2.2 Atmospheric Equations

In atmospheric dynamics, the vorticity, $\boldsymbol{\zeta} = \nabla \times \boldsymbol{u}$, is generally considered a more informative property of the fluid to study since it is this that drives the change in energy of the fluid [4]. That is, since vorticity is the measure of fluid rotation around a fixed axis allows for the movement of momentum, energy and mass throughout the fluid by vortices which carry these properties as they move, twist and stretch within the fluid.

We can write the vorticity formulation of the above by taking the curl of (2.4),

$$\begin{aligned} &\nabla \times \left[\frac{\partial \boldsymbol{u}}{\partial t} + (\boldsymbol{u} \cdot \nabla)\, \boldsymbol{u} = -\frac{1}{\rho_0}\nabla p' + \nu \nabla^2 \boldsymbol{u} + \frac{\rho'}{\rho_0} g \hat{\boldsymbol{z}} \right] \\ \Rightarrow &\frac{\partial \boldsymbol{\zeta}}{\partial t} + (\boldsymbol{u} \cdot \nabla)\, \boldsymbol{\zeta} = (\boldsymbol{\zeta} \cdot \nabla)\, \boldsymbol{u} + \left(\frac{\partial \theta}{\partial y}, -\frac{\partial \theta}{\partial x}, 0 \right) + Re^{-1}\nabla^2 \boldsymbol{\zeta} \end{aligned} \tag{2.7}$$

The pressure term, ∇p, disappears since the curl of the gradient is zero. A quantity closely related to the vorticity is that of enstrophy.

The total enstrophy of the system, Ens, is defined as half the integral of vorticity squared, that is,

$$\text{Ens} = \frac{1}{2}\int_{\mathscr{D}} \boldsymbol{\zeta}^2 d\mathscr{D} \equiv \int_x \int_y \int_z \boldsymbol{\zeta}^2 dx dy dz \tag{2.8}$$

provided that the incompressibility condition, $\nabla \cdot \boldsymbol{u} = 0$, holds. We allow ourselves to be restricted by the incompressibility condition since our topic of study is modelled as an incompressible geophysical fluid, more generally, without the use of

incompressibility, one would define total enstrophy as,

$$\int_{\mathscr{D}} |\nabla \boldsymbol{u}|^2 \, d\mathscr{D}$$

where, in the above, $|\cdot|$ is a Frobenius norm.

Given the vorticity equation, (2.7), we can take the dot product with vorticity and it to give the (local) enstrophy equation,

$$\frac{1}{2}\frac{\partial \boldsymbol{Z}}{\partial t} + \frac{1}{2}\left(\boldsymbol{u}\cdot\nabla\right)\boldsymbol{Z} = \underbrace{\sum_{i=1}^{3}\sum_{j=1}^{3}\zeta_i S_{ij}\zeta_j}_{\text{vortex stretching}} + \underbrace{\hat{\boldsymbol{z}}\cdot\left(\boldsymbol{\zeta}\times\nabla\theta\right)}_{\text{baroclinic production}} + \underbrace{\frac{1}{Re}\left(\boldsymbol{\zeta}\cdot\nabla^2\boldsymbol{\zeta}\right)}_{\text{viscous effects}} \tag{2.9}$$

where S_{ij} is the rate of strain tensor given by

$$S_{ij} = \frac{1}{2}\left(\frac{\partial u_i}{\partial x_j} + \frac{\partial u_j}{\partial x_i}\right)$$

and $\hat{\boldsymbol{z}}$ the unit vector in the z direction.

The rate of change of enstrophy equation, (2.9), contains terms that positively contribute to it. We will use these 'enstrophy production' terms, of *vortex stretching* and *baroclinic production*, later in order to explain the growth in enstrophy due a developing instability.

Another quantity that will prove useful to study is the energy, comprised of kinetic energy and potential energy. The kinetic energy equation is obtained by multiplying (2.4) by the velocity, $\boldsymbol{u}$,

$$\begin{aligned}
&\boldsymbol{u}\cdot\left[\frac{\partial \boldsymbol{u}}{\partial t} + \left(\boldsymbol{u}\cdot\nabla\right)\boldsymbol{u} = -\frac{1}{\rho_0}\nabla p + \theta\hat{\boldsymbol{z}} + Re^{-1}\nabla^2\boldsymbol{u}\right] \\
\Rightarrow &\frac{1}{2}\frac{\partial \boldsymbol{u}^2}{\partial t} + \left(\boldsymbol{u}\cdot\nabla\right)\frac{\boldsymbol{u}^2}{2} = -\frac{\boldsymbol{u}}{\rho_0}\nabla p + w\theta + Re^{-1}\nabla\cdot\left(\boldsymbol{u}\nabla\boldsymbol{u}\right) - Re^{-1}\left(\nabla\boldsymbol{u}\right)^2
\end{aligned} \tag{2.10}$$

using the identity $\nabla\cdot(\boldsymbol{u}\nabla\boldsymbol{u}) = \boldsymbol{u}\nabla^2\boldsymbol{u} + (\nabla\boldsymbol{u})^2$ and where w is the vertical component of the velocity. Similarly, the potential energy equation is obtained by taking the

product of (2.5) with the potential temperature, θ,

$$\begin{aligned} &\theta \cdot \left[\frac{\partial \theta}{\partial t} + (\boldsymbol{u} \cdot \nabla)\, \theta = \kappa \nabla^2 \theta \right] \\ \Rightarrow &\frac{1}{2} \frac{\partial \theta^2}{\partial t} + (\boldsymbol{u} \cdot \nabla)\, \frac{\theta^2}{2} = \kappa \nabla \cdot (\theta \nabla \theta) - \kappa \left(\nabla \theta \right)^2 \end{aligned} \tag{2.11}$$

again using the identity $\nabla \cdot (\theta \nabla \theta) = \theta \nabla^2 \theta + (\nabla \theta)^2$.

Potential vorticity is a quantity that serves useful in marking certain points in the fluid since it is advected with it. The vorticity of fluid may change if it is stretched or compressed, however if the absolute vorticity is normalised by the length scale of the spacing of potential temperature isosurfaces, the result is a locally conserved quantity termed potential vorticity and defined as

$$PV = \boldsymbol{\zeta} \cdot \nabla \theta$$

Potential vorticity acts as a flow tracer which we will use to indicate regions of high vorticity production and their positions within the fluid.

Chapter 3

The Zigzag Instability

The zigzag instability is characterised by the twisting and bending of the entire columnar vortex with next to no change to the cross sectional structure of the dipole. It is thought that this bending of the vortex is the origin of the layering observed in stratified turbulent flows. It is known that fluid motions in the atmosphere, which are affected by stable density stratification, have large vertical motions inhibited by the buoyancy force [2]. Numerical and experimental studies have shown that these vortices do not have large vertical reach [15, 16]. Instead it appears that they look like thin 'pancakes.' Because of the strong vertical shear induced between vertically neighbouring pancake vortices, it has been shown that energy dissipation is enhanced [17, 18]. It is this feature of enhanced energy dissipation that it is suspected to be the reason as to why stratified turbulence differs so profoundly from two-dimensional turbulence.

This zigzag instability, which causes the horizontal decoupling of the vortex, is unique from both the Crow and elliptic instability which may occur in homogeneous fluid. With strongly stratified fluid, and where buoyancy effects are dominant, both the Crow and elliptic instabilities are inhibited, but yet the columnar vortex is sliced into thin horizontal layers of pancake like dipoles. The cause of this being the new type of instability: zigzag instability.

The feedback mechanism that allows for the growth of the zigzag instability begins with the initial bending of the vortex column, causing the temperature scalar to have a large gradient in the corners of the zigzag. This large scalar gradient allows for the initial growth in baroclinic production of enstrophy by pulling the vortex column outward in the direction of propagation. This makes this portion of the vortex column nearly horizontal in the region between its original position and the corners of the zigzag. This interaction leads to strong flattening of the vortices perpendicular to the direction of propagation, increasing the gradient of the scalar further and hence completing a feedback loop that allows the instability to grow.

The inhibition of the Crow instability due to stratification has been shown by Williamson and Chomaz (1997, [19]) for a Froude number of order unity. The elliptic instability, on the other hand, under the gravitational restoring force caused the three dimensional motion to collapse into a re-laminarised vortex pair which then cause the formation of pancake vortices in the flow. In the presence of stratification it is possible to inhibit also the elliptic instability with careful choices for the Brunt-Väisälä frequency and Froude numbers (Froude number less than one) [12, 20].

The first experiment that was performed with the specific aim of developing the zigzag instability was by Billant and Chomaz (2000, [2]) in which, in a tank filled a stratified salt solution, two counter rotating columnar vortices were created by rapidly closing two vertical flaps. The vortices were made visible by the use of a fluorescent dye. Some images from this experiment are reproduced in Fig. 3.1, the images are shown as though the vortex columns are propagating out of the page, i.e. in the $y - z$ plane.

After having observed the zigzag instability experimentally, the same authors have presented a series of papers studying the zigzag instability theoretically [11, 20, 21, 22] and numerically [3, 12, 20, 23, 24]. However, it is the discrepancies between the experimental and numerical results that form part of the motivation behind this thesis. The primary difference observed between the experimental results [2] and

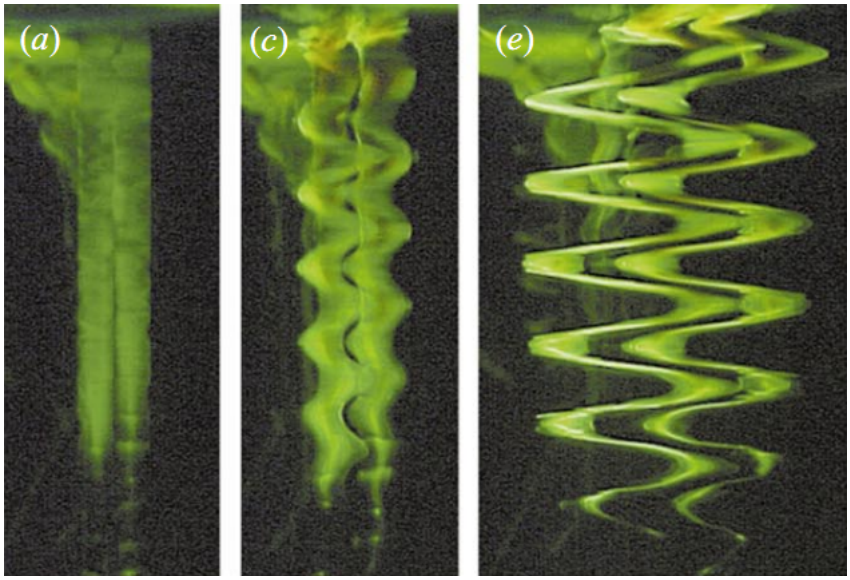

Figure 3.1: Growth of the zigzag instability, frontal views taken at 7, 36 and 75 seconds. Reproduced from Billant and Chomaz (2000, [2])

the numerical simulations [3] is; in the experimental results it was observed that the growth in zigzag instability peaks at $t = 35$ whereas the corresponding peak in the numerical simulations occurs at $t = 92$. We see in §4.4 that in order to achieve results closer to that of the experimental work, one must consider an entirely new family of initial conditions.

We will first show agreement with the numerical results [3], for validation purposes, and then propose alternate initialisations of the vortex columns that will become unstable to the zigzag instability faster. These alternate initial conditions address a limitation in the method Billant and Chomaz use to initialise their perturbed vortex columns. Billant and Chomaz choose to initialise their simulations with two vortex columns in a stratified fluid with a sinusoidal type perturbation applied to the vertical velocity field [3], this however limits the perturbation to act on the same horizontal plane on both vortex columns and further acts over the entire vortex column. We address this by choosing to perturb the vorticity rather than the velocity, this has the advantage of allowing the perturbations applied to the two vortex columns to be independent of each other. We discuss this further in the next

chapter.

Chapter 4

Numerics

Direct numerical simulation was carried out using the parallelised fortran code of Robert M. Kerr [25].

4.1 Numerical Scheme

The vorticity formulation of the Navier-Stokes Boussinesq equations (2.7) are solved in a box periodic in each direction, x, y and z. The non-linear terms are solved using a pseudo-spectral method with time advancement calculated by a third order explicit Runga Kutta method. The Runga Kutta method, being a single step advancement method rather than a multistep one, has the advantage of begin self-starting, this allows for calculations to be stopped and saved at a certain time step from which one is able to resume the calculation. Viscous terms are solved using an integrating factor rather than the Crank-Nicolson method. Aliasing is dealt with by truncating 1/3 of the modes in each direction, the first and last sixths. Aliasing is required in pseudo-spectral methods else without which high wavenumber errors accumulate polluting the solution.

Calculations were performed using 16 cores and 16GB of RAM from the (now decommissioned) computing cluster at Warwick University, known internally as

Francesca. Francesca was a 960 core high bandwidth and low latency Linux cluster of 3GHz Intel Xeon processors.

4.2 Numerical Simulations

We begin by reproducing the numerical results obtained by Deloncle et al. [3] in order to verify the numerics. We define non-dimensional parameters, Froude number and Reynolds number, as in [2]

$$Fr = \frac{U}{Nr} , \quad Re = \frac{Ur}{\nu} \tag{4.1}$$

where U is the initial propagating speed of the vortex columns, N the Brunt Väisälä frequency,

$$N^2 = \frac{-g}{\rho}\frac{\partial \rho}{\partial z}$$

r the initial vortex column radius and ν the viscosity.

Physically, the Reynolds number is a measure of the importance of speed over viscous forces. At low speeds viscous forces dominate resulting in a small Reynolds number, where as a large Reynolds number indicates the dominance of the fluid inertia over the viscous forces. The Brunt Väisälä frequency provides a description of the stability of the stratification of the fluid. A fluid parcel perturbed vertically in a stratified fluid will accelerate vertically either back toward its initial position or away from it. In the first instance, stratification is stable and $N^2 > 0$, else if the parcel accelerates away from its initial position then the stratification is unstable.

The dependence of the onset of the zigzag instability on the Froude number has been studied in [11, 23] where it has been found that in order for the zigzag instability to evolve, it is required that $Fr < 1$. Hence, for all numerics that follow, we choose

$$Fr = \frac{2.19}{2.41 \times 1.32} = 0.69 , \quad Re = \frac{2.19 \times 1.32}{0.0025} = 1152$$

This compares well with the direct numerical simulation performed by Deloncle et al. [3, pp. 231] in which $Fr = 0.66$ and $Re = 1060$.

4.3 Reproduction of Previous Results

The direct numerical simulation carried out by Deloncle et al. [3] to simulate the zigzag instability begins with two counter rotating vortex columns with a Gaussian vortex core profile. In order to perturb the vortex columns the velocity field is initialised as the sum of a two dimensional flow along with a sinusoidal velocity profile for z (see [3, pp. 230] for details). The numerical results presented in [3, Fig. 1] of vorticity isosurfaces are reproduced in Fig. 4.1 for later comparison.

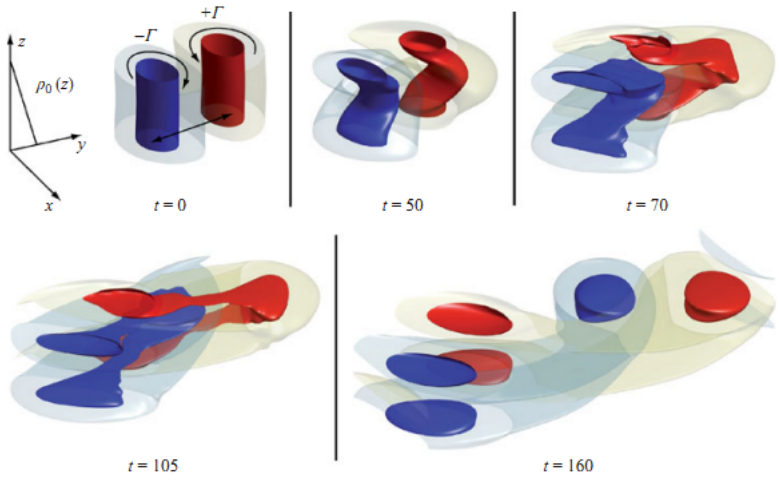

Figure 4.1: Vorticity isosurfaces of simulation with $Fr = 0.66$ and $Re = 1060$. Red and blue contours are 60% of vertically averaged maximum vertical vorticity. Reproduced from Deloncle et al. [3, Fig. 1, pp.231]

Rather than choosing to perturb the velocity field it was chosen to perturb the vortex columns themselves (see §4.4). Hence, for this case of verification, the vorticity profile of the vortex columns were perturbed sinusoidally in the y direction, this is the direction perpendicular to the direction of vortex propagation which occurs in x. Additionally, the sinusoidal perturbation was applied equally to both of the vortex columns, as such the point of maximum perturbation occurs on the

same horizontal plane. This initial vortex column profile is shown in the first frame of Fig. 4.2.

The scalar, θ, is initialised as a linearly varying vertical temperature gradient, it itself is not directly perturbed initially.

The parameters used for the computational domain ($\mathscr{D}$) are $(L_x, L_y, L_z) = 2\pi \times (2, 4, 2)$ with the number of mesh points in the x, y and z direction, $(N_x, N_y, N_z) = (128, 256, 256)$. The Prandtl number, Pr, is set to unity, the Brunt Väisälä frequency, $N = 2.41$ and the viscosity $\nu = 0.0025$.

The vortex columns are initialised such that the magnitude of the circulation, $|\Gamma| = 10.06$, with the columns counter rotating ($\Gamma_1 = -\Gamma_2$). The vortex core radii are $r = 1.32$ and the centres of the vortex columns are separated by a distance, $a = 2.34$. A characteristic time scale unit is defined by

$$\frac{2\pi r^2}{|\Gamma|}$$

The evolution of enstrophy for this initial profile is shown in Fig. 4.2. Flattening of the vortex at the points of maximum perturbation can first be observed at $t = 12$. By $t = 24$ this flattening is pronounced and at the point which the vortex column bends it has become stretched out further away from the central line of the vortex column (the vertical line joining the centre of the vortex at the top of the column to the centre of the vortex at the bottom of the column). This stretching and flattening continues and by $t = 42$ discrete 'pancakes' of enstrophy can be seen. The characteristic profile of the zigzag instability, as seen in Fig. 3.1 [2], can be more clearly seen in Fig. 4.3. The distinct behaviour of the zigzag instability generating thin horizontal layers of vorticity can be seen by $t = 54$ and is clearly demonstrated in the $t = 78$ frame.

One can measure the growth of the zigzag instability by calculating the enstrophy through time. The enstrophy, being essentially a measure of the vorticity of the

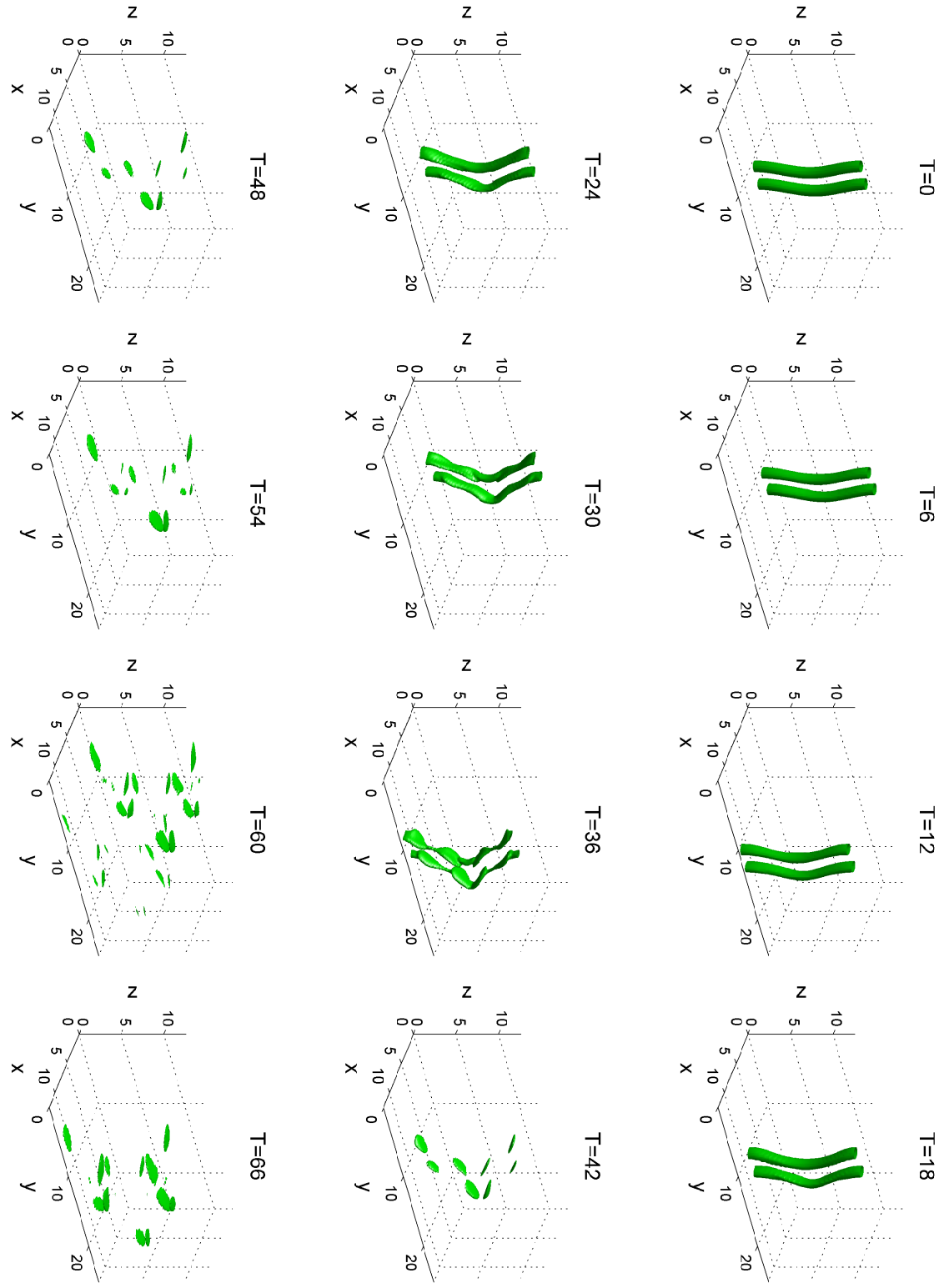

Figure 4.2: Evolution of the pair of vortex columns which began with a sinusoidal perturbation applied perpendicular to the direction of propagation.

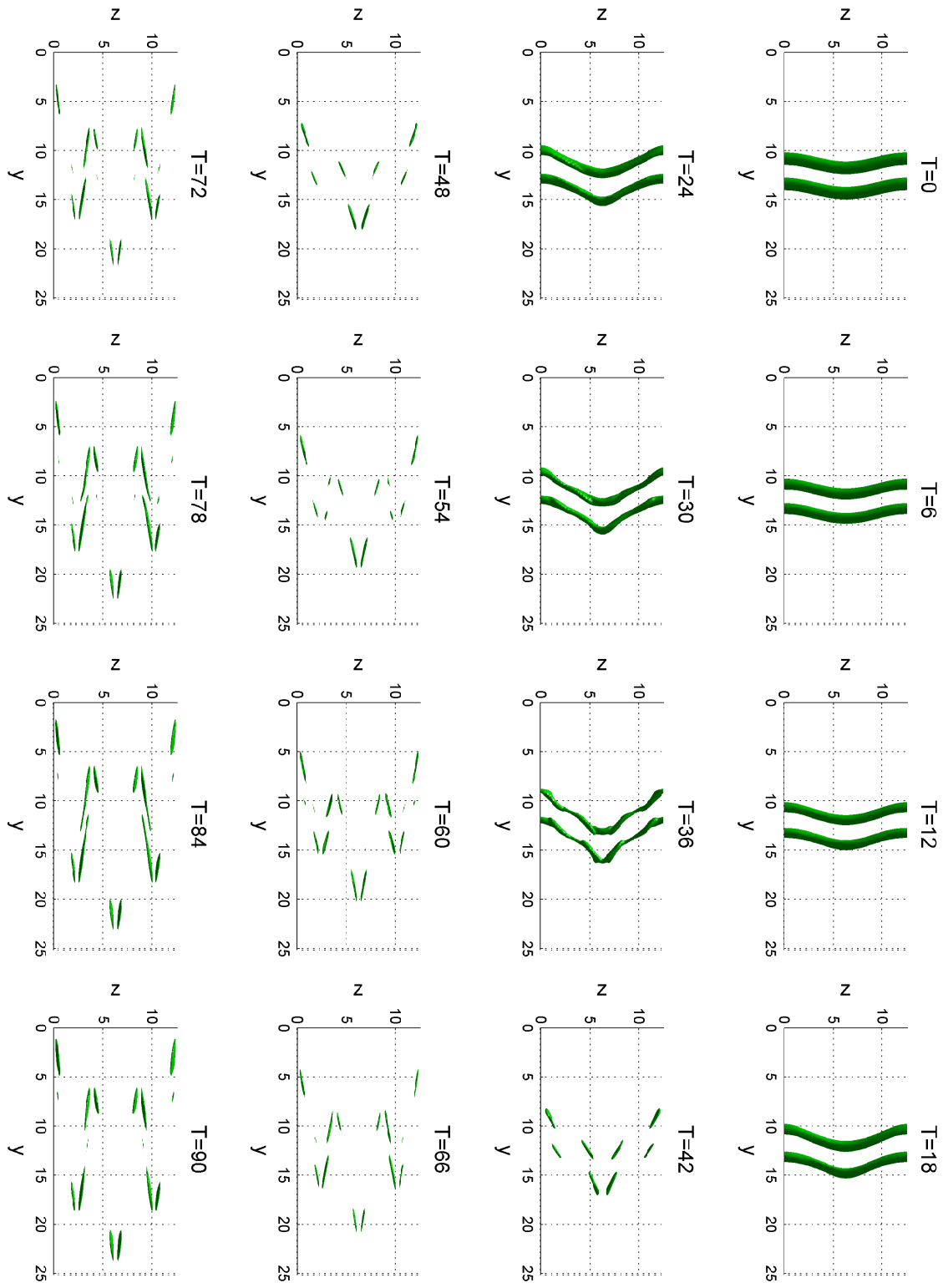

Figure 4.3: Evolution of the pair of vortex columns, in the $y - z$ plane, with the initial sinusoidal perturbation applied.

system, will grow as the vorticity increases due to vorticity production by stretching and baroclinic production. As vorticity dissipates due to the viscosity, the enstrophy will also reduce. Further, since enstrophy derives from derivatives of energy, and the integral value of energy is bounded from above, increasing enstrophy is a signature of the generation of large derivatives of the velocity, which in Fourier space implies the velocity and energy have cascaded to higher wavenumbers (smaller length scales).

Figure 4.5 shows the enstrophy in each direction, x, y and z as well as the sum total enstrophy through time. We observe that initially the total enstrophy in the system is 0.169 which is entirely contained within the z component of enstrophy. This z component of enstrophy $\left(Z_z = \hat{\boldsymbol{z}} \int_{\mathscr{D}} \boldsymbol{\zeta}^2 d\mathscr{D}\right)$ dissipates almost linearly till $t = 40$. Between $t = 40$ and $t = 64$, Z_z dissipates slightly faster than in the initial period of dissipation, after which, the rate of dissipation slows and z enstrophy dissipates exponentially slowly. The remaining two components of enstrophy, Z_x and Z_y, which initially begin at zero both grow exponentially quickly till $t = 60$ where they attain their respective peak values of 0.071 and 0.21. After reaching these peak values, these x and y enstrophy components dissipate away exponentially, although in the case of Z_y not as quickly as the enstrophy grew. The total enstrophy in the system is dominated by the horizontal components of enstrophy and more specifically Z_y. Total enstrophy decays slightly as Z_z decays and whilst Z_y is still in a slow growth phase, however once the y component of enstrophy begins exponential growth in earnest, at $t = 20$, total enstrophy grows exponentially reaching its peak value of 0.32 at $t = 60$. This is an increase of 1.85 times the initial value of total enstrophy. Enstrophy reaches a peak value after which it decreases, rather than continuing to grow, due to viscous dissipation. As the vortex sheets flatten their length scale decreases to a value at which the viscous effects of the fluid dominate the inertia and thus dissipate the vorticity away rather than allowing it to continue growing and thus breaking the feedback loop of the zigzag instability.

These profiles of enstrophy evolution agree with those observed by Deloncle et

al. [3, Fig. 2(b)] which is reproduced for comparison in Fig. 4.4.

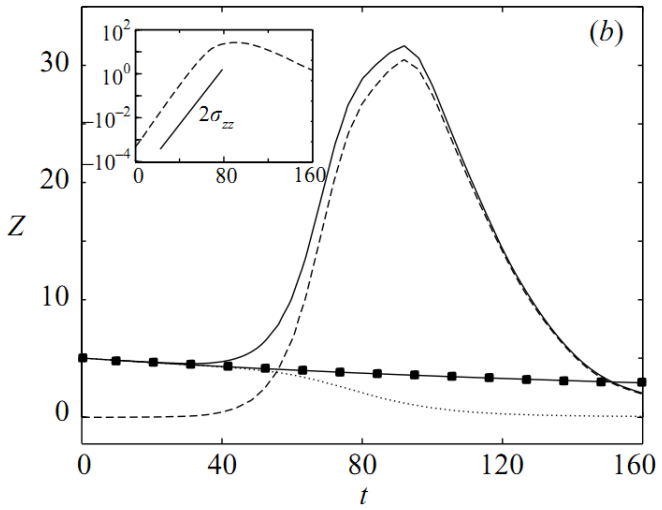

Figure 4.4: Enstrophy evolutions of run $Fr = 0.66$, $Re = 1060$. Total enstrophy Z (solid line), horizontal enstrophy Z_h (dashed line). Reproduced from Deloncle et al. [3, Fig. 2(b), pp.232]

Given we are satisfied that we have reproduced previous work on characterising the zigzag instability, our aim is now to devise a new scenario in which the zigzag instability is able to develop and grow more rapidly than that previously seen. We propose four new initial vortex column profiles which differ by their direction of perturbation and by the horizontal plane on which the perturbation is applied on each column.

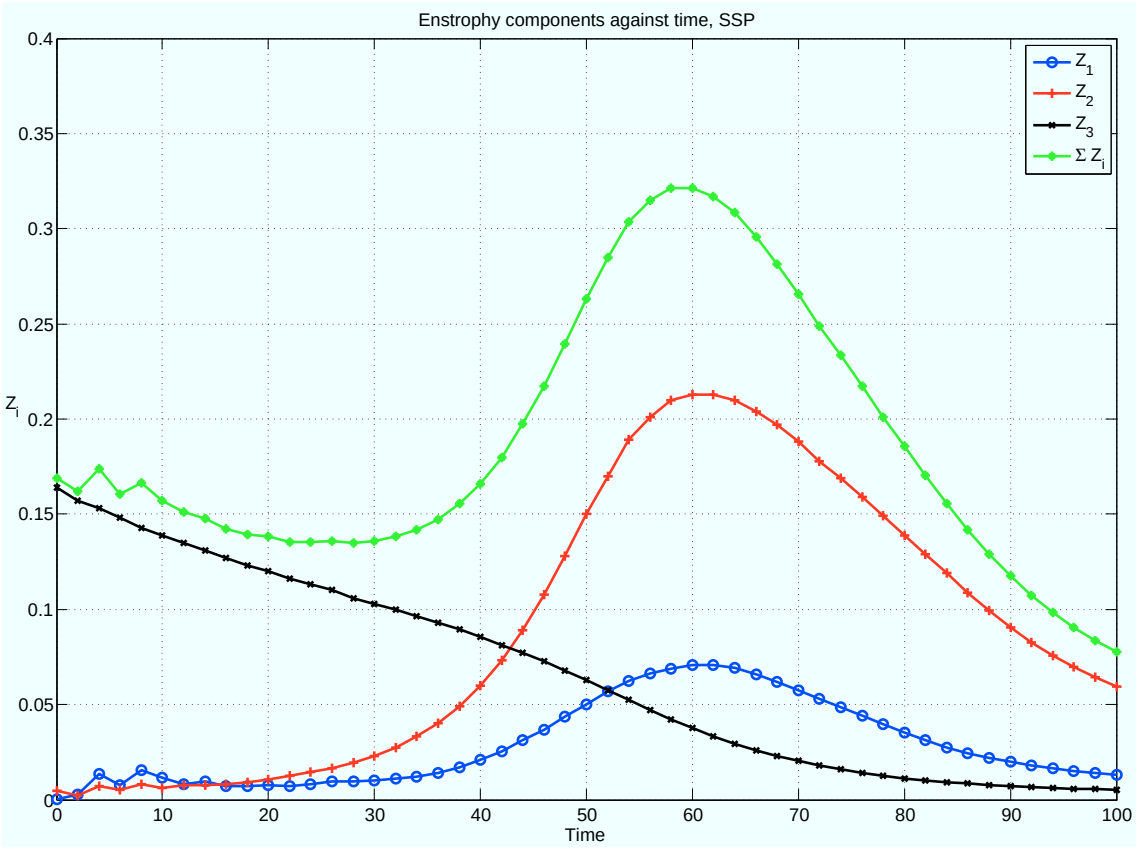

Figure 4.5: Change through time of the three components of enstrophy and their sum for the initial profile with the sinusoidal perturbation.

4.4 Proposal for More Unstable Initial Profiles

We wish to speed up the onset and growth of the zigzag instability such that we may obtain enstrophy growth, magnitude and onset time, matching closer to that of the experimental results in Billant and Chomaz (2000, [2]) than had been obtained in previous numerical simulations [3]. We aim to achieve this by considering four variations of vortex columns with perturbations. The first important difference between these new profiles and the sinusoidally perturbed profile seen previously are that the perturbations are now applied much more locally within the vortex column. Where previously the reach of the sinusoidal perturbation was over the entire vortex column, only the central third of the column is now perturbed. This localisation of the perturbation to the central section of the vortex column was

found to lead to the onset of the zigzag instability faster than if the perturbations were applied over the entire column. The desire to perturb the vortex columns with the perturbations on each column offset from the other explains the choice made to perturb the vortex column itself rather than the velocity field; it would not be possible to apply non-symmetric perturbations to the overall velocity.

Along with the localisation of the perturbation, we define four initial conditions,

1. Perturbation applied in the direction of propagation and not in the same horizontal plane

2. Perturbation applied in the direction perpendicular to propagation and on the same horizontal plane

3. Perturbation applied in the direction perpendicular to propagation and not in the same horizontal plane

4. Perturbation applied in the direction of propagation and on the same horizontal plane

which are summarised in table 4.1 and shown pictorially in Fig. 4.6. These orientations of vortex column perturbations were chosen based on trying to understand the reason behind why the experimental results [2] become unstable much quicker than those seen in prior numerical simulation [3]. For example, the centre frame of Fig. 3.1 (reproduced from [2]) is taken at $t = 36$ where as a similar scenario takes at least till $t = 50$ in the numerical simulations of Deloncle et al. [3, Fig. 1]. It was proposed that a more physically realistic scenario would be of two vortex columns meeting which do not have perfectly symmetric perturbations. Hence we choose to initialise with perturbations that are both offset and coplanar.

For the purposes of later brevity we shall use the following abbreviations for the different initial conditions,

	Perturbation	
	Parallel	Perpendicular
Coplanar	CPa	CPe
Offset	OPa	OPe

If we define the unique point on the vortex column that is on the perturbation and is the furthest horizontal distance from the vortex centre as $(x_{1,2}, y_{1,2}, z_{1,2})$, where subscripts $1, 2$ denote the left and right vortex respectively, then the four simulations to run can be summarised by,

	Perturbation	
	Parallel	Perpendicular
Coplanar	$z_1 = z_2$ $x_1 = x_2$ $\min\left[\mathbf{C} - (x_{1,2}, y_{1,2}, z_{1,2})\right] = \hat{\mathbf{x}}d$	$z_1 = z_2$ $x_1 = x_2$ $\min\left[\mathbf{C} - (x_{1,2}, y_{1,2}, z_{1,2})\right] = \hat{\mathbf{y}}d$
Offset	$z_1 \neq z_2$ $x_1 = x_2$ $\min\left[\mathbf{C} - (x_{1,2}, y_{1,2}, z_{1,2})\right] = \hat{\mathbf{x}}d$	$z_1 \neq z_2$ $x_1 = x_2$ $\min\left[\mathbf{C} - (x_{1,2}, y_{1,2}, z_{1,2})\right] = \hat{\mathbf{y}}d$

Table 4.1: Summary of the four initial vortex column profiles considered.

where $\mathbf{C}$ is the line following the centre of the vortex column, $\hat{\mathbf{x}}$, $\hat{\mathbf{y}}$ are unit vectors in the x and y direction respectively and d some constant measuring the size of the perturbation.

Figures 4.7 to 4.10 show enstrophy isosurfaces of the vortex columns for each of the four initial conditions through time. Isosurfaces for potential vorticity are also overlaid on enstrophy isosurfaces, with red being areas of positive potential vorticity and blue areas of negative potential vorticity. In each of the four figures, one can observe the formation of the zigzag instability, albeit at different time points. The formation of the zigzag instability is similar to that seen in Fig. 4.2. Initially the vortex columns align themselves such that the perturbation is in the y direction, after which the corners of the perturbation pull away from the vortex column, stretching and flattening out the part of the column in-between these corners. This process

of stretching and flattening continues until discrete vortex layers are visible which then further breakdown into discrete 'pancakes' of enstrophy. It is also observed that potential vorticity concentrates itself in the corners of the perturbations with the vortex columns, that is, it is in these corners that the baroclinic production of vorticity, of either sign, is large. These areas of potential vorticity remain stably at the corners of the perturbation and hence serve as a good visible marker for these perturbation corners. This is especially helpful for initial profiles which give rise to multiple zigzag instabilities as time proceeds for which pairs of red and blue (positive and negative) potential vorticity isosurfaces serve as a quick indication of the number of zigzag instabilities developed within the column. Figures 4.11 to 4.14 show the same four simulations enstrophy isosurfaces but in the $y - z$ plane, the view of the vortex columns propagating out of the page. These figures give a clearer indication of when the instability begins to develop and also the stretching of the perturbation corners away from the initial vortex position. Visually these simulations continue to agree well with the experimental results [2] reproduced in Fig. 3.1 with the vortex columns bending to form a zigzag which then flattens out stretching away from the vortex core to leave the distinctive sharp zigzags in the vortex column.

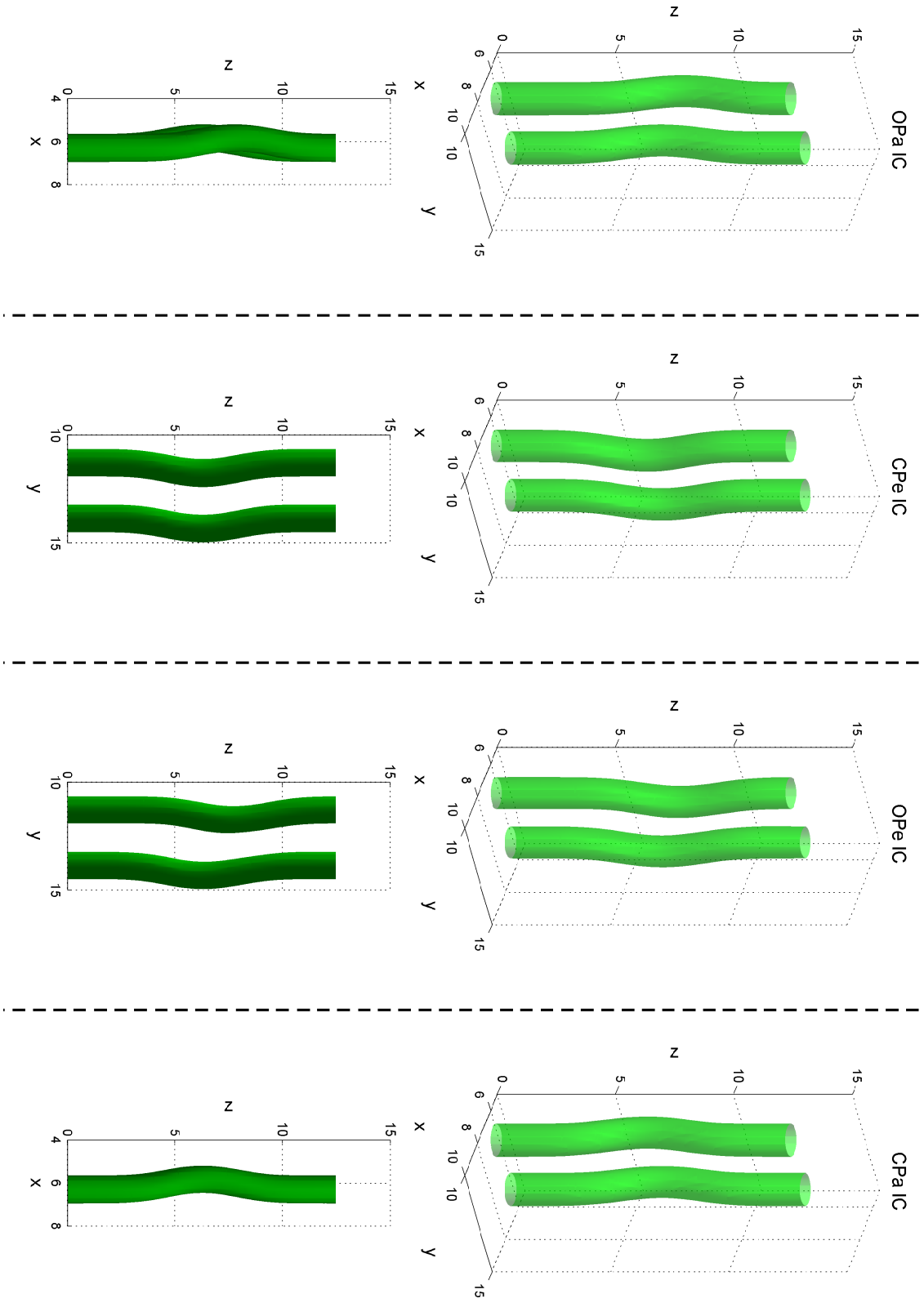

Figure 4.6: Views of the four different new initial conditions proposed to be more unstable to the zigzag instability.

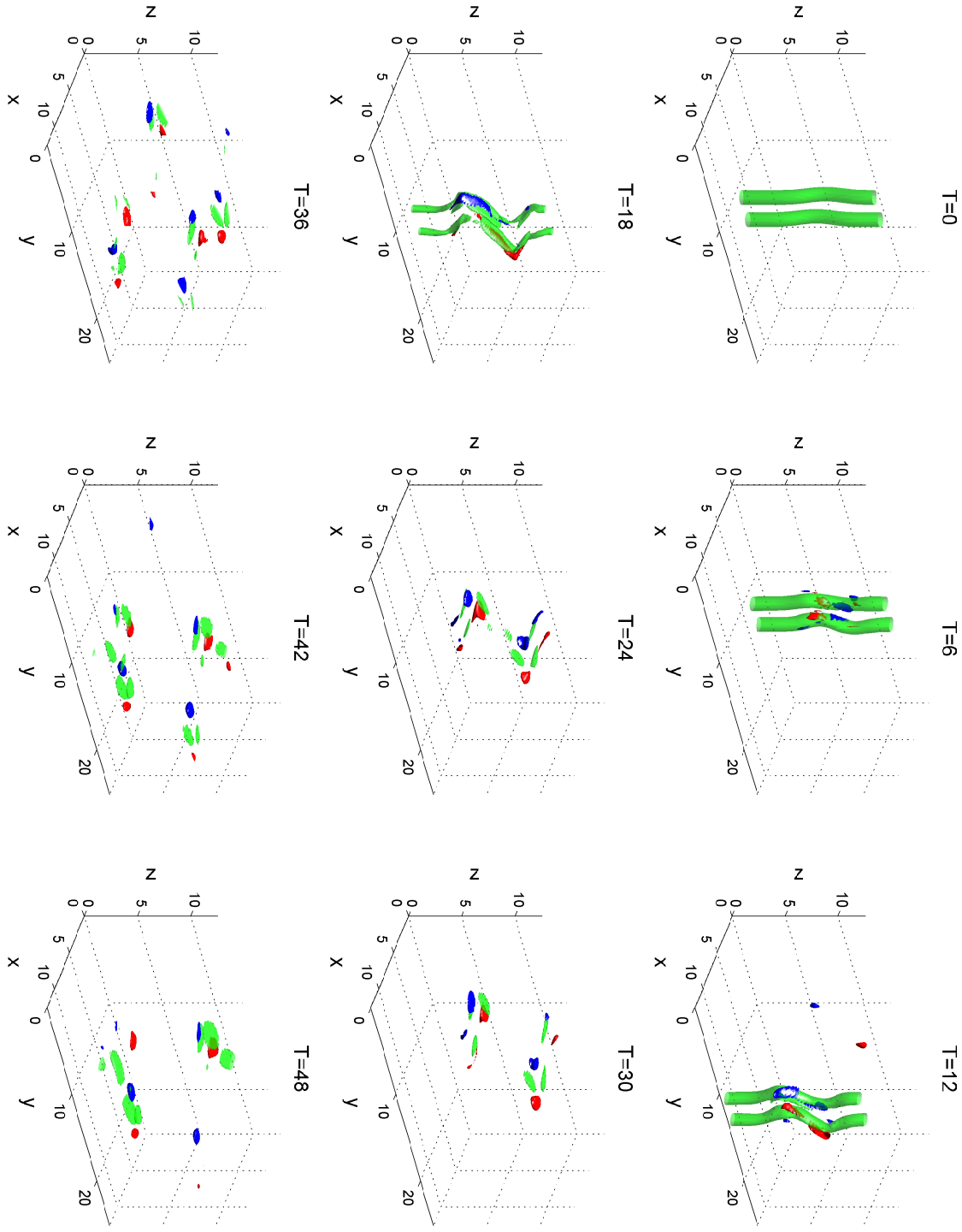

Figure 4.7: Evolution of the pair of vortex columns which began with an offset perturbation parallel to the direction of travel. The red and blue surfaces are areas of positive and negative potential vorticity. The PV isosurface thresholds are, in red $0.55 \cdot \max_{\boldsymbol{x} \in \mathscr{D}} (PV)$ and in blue the negative of the same value.

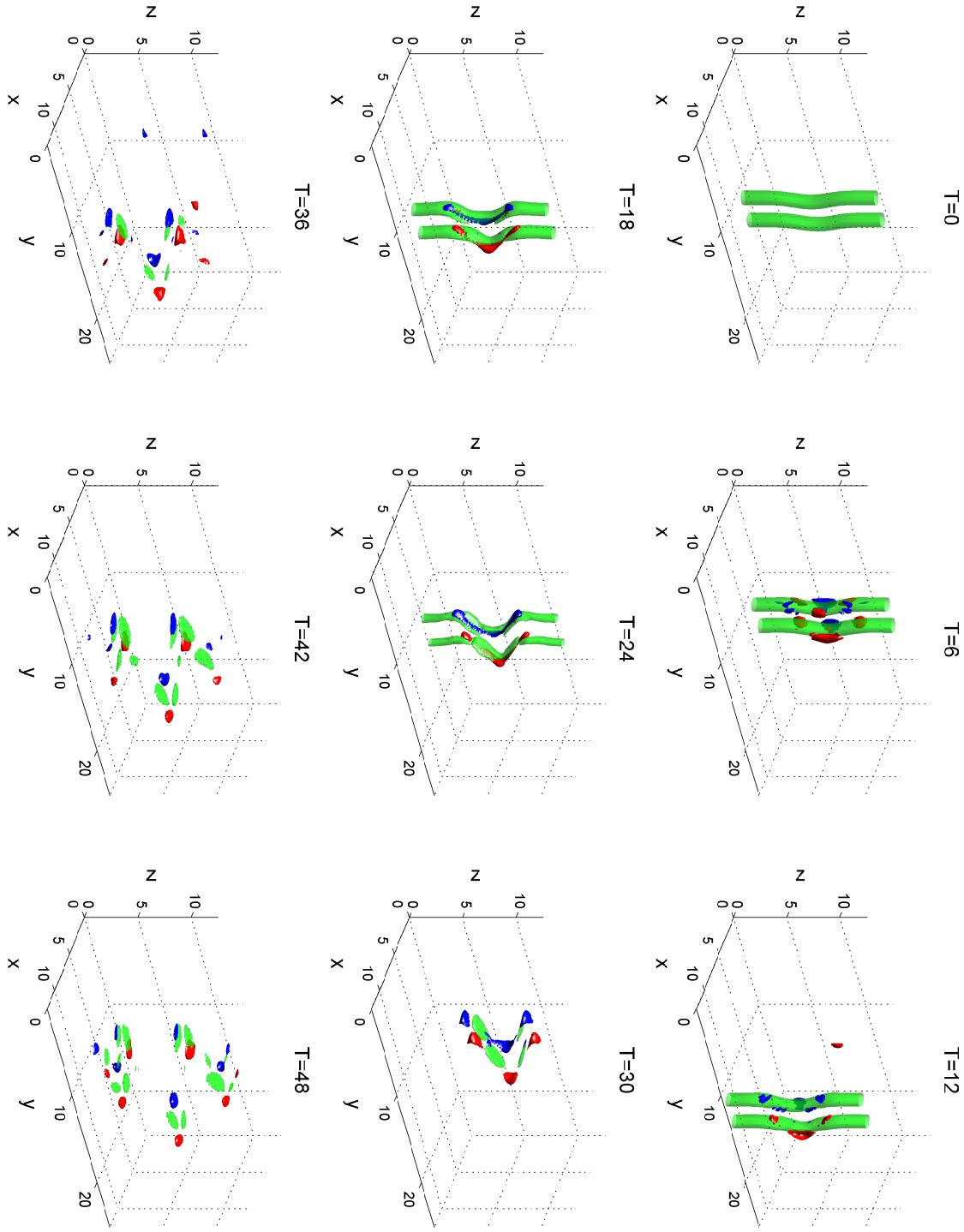

Figure 4.8: Evolution of the pair of vortex columns which began with a coplanar perturbation perpendicular to the direction of travel. Red and blue surfaces of PV defined as in Fig. 4.7.

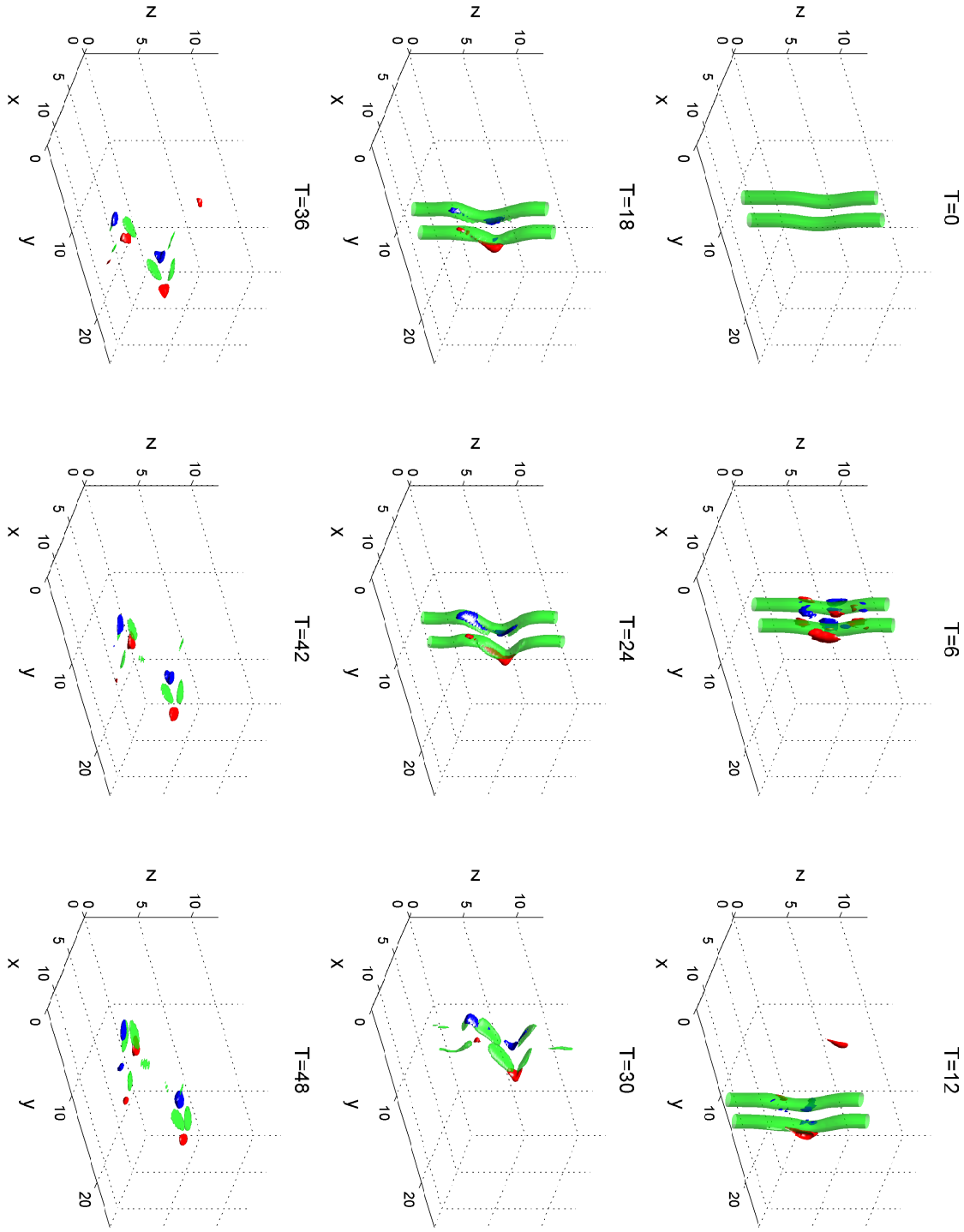

Figure 4.9: Evolution of the pair of vortex columns which began with an offset perturbation in the direction of travel. Red and blue surfaces of PV defined as in Fig. 4.7.

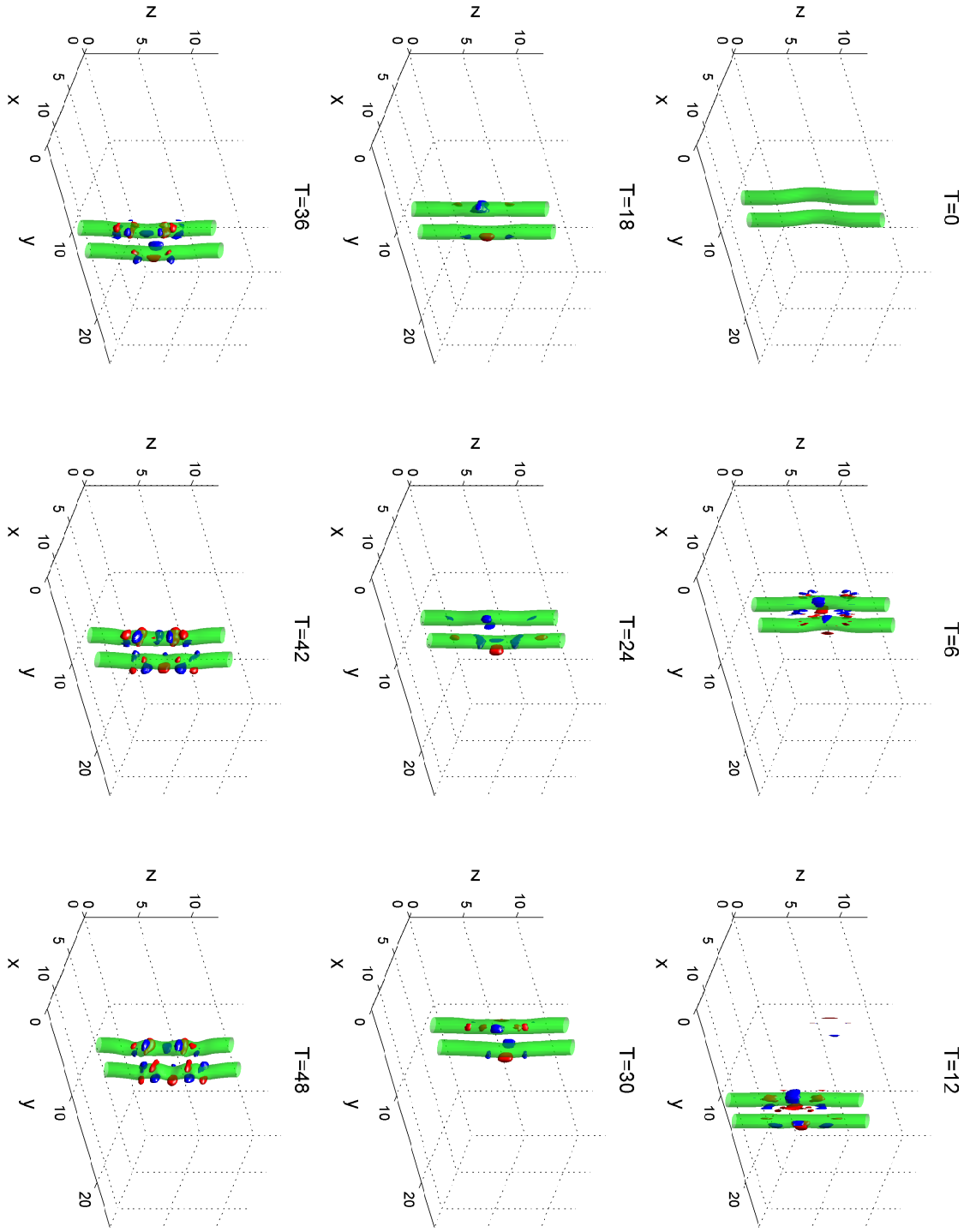

Figure 4.10: Evolution of the pair of vortex columns which began with a coplanar perturbation in the direction of travel. Red and blue surfaces of PV defined as in Fig. 4.7.

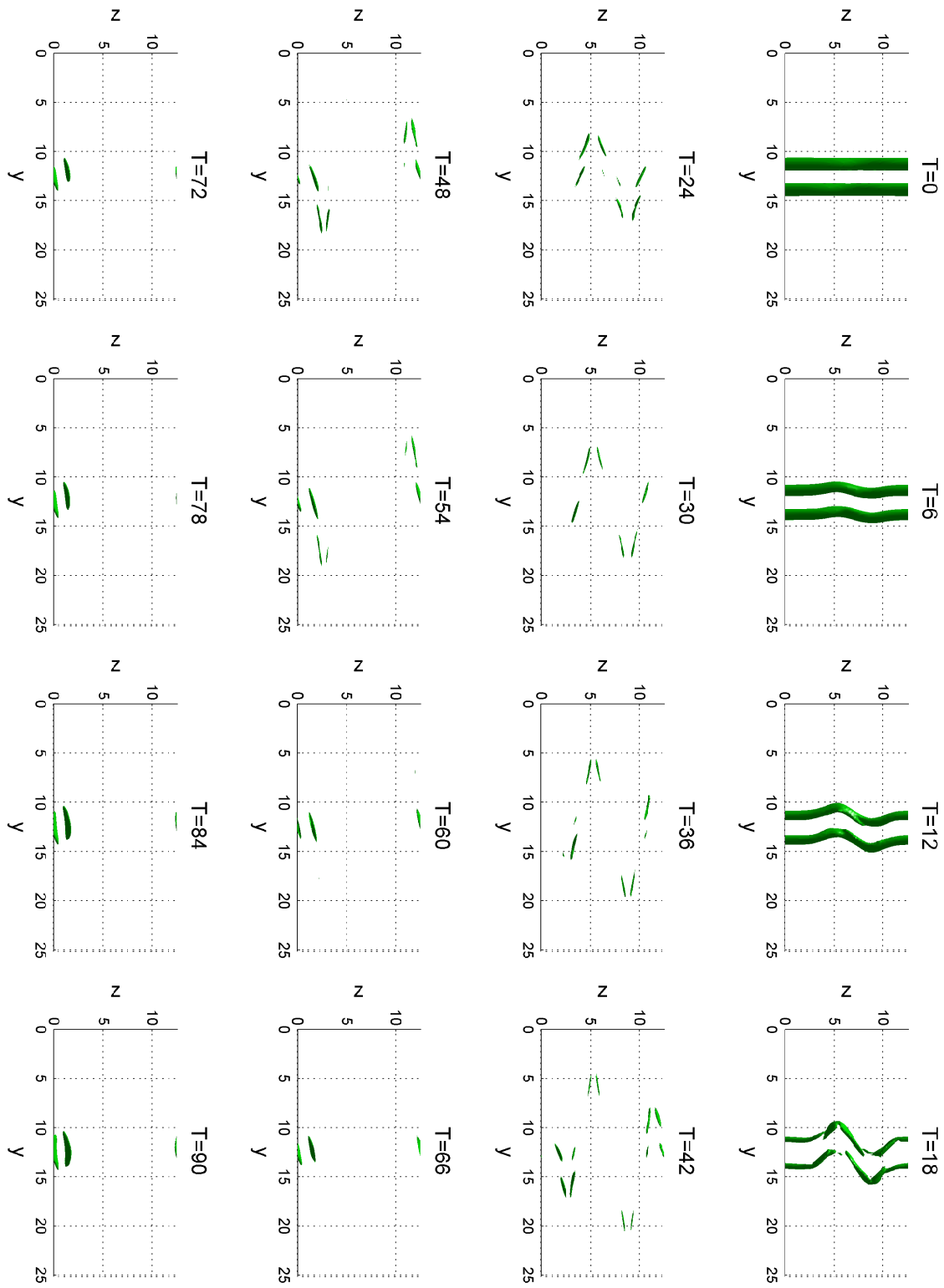

Figure 4.11: Evolution of the pair of vortex columns, in the $y-z$ plane, with the perturbation applied offset in the direction of travel. Enstrophy isosurface value taken as $0.5 \cdot \max_{\boldsymbol{x} \in \mathscr{D}} (\boldsymbol{Z})$.

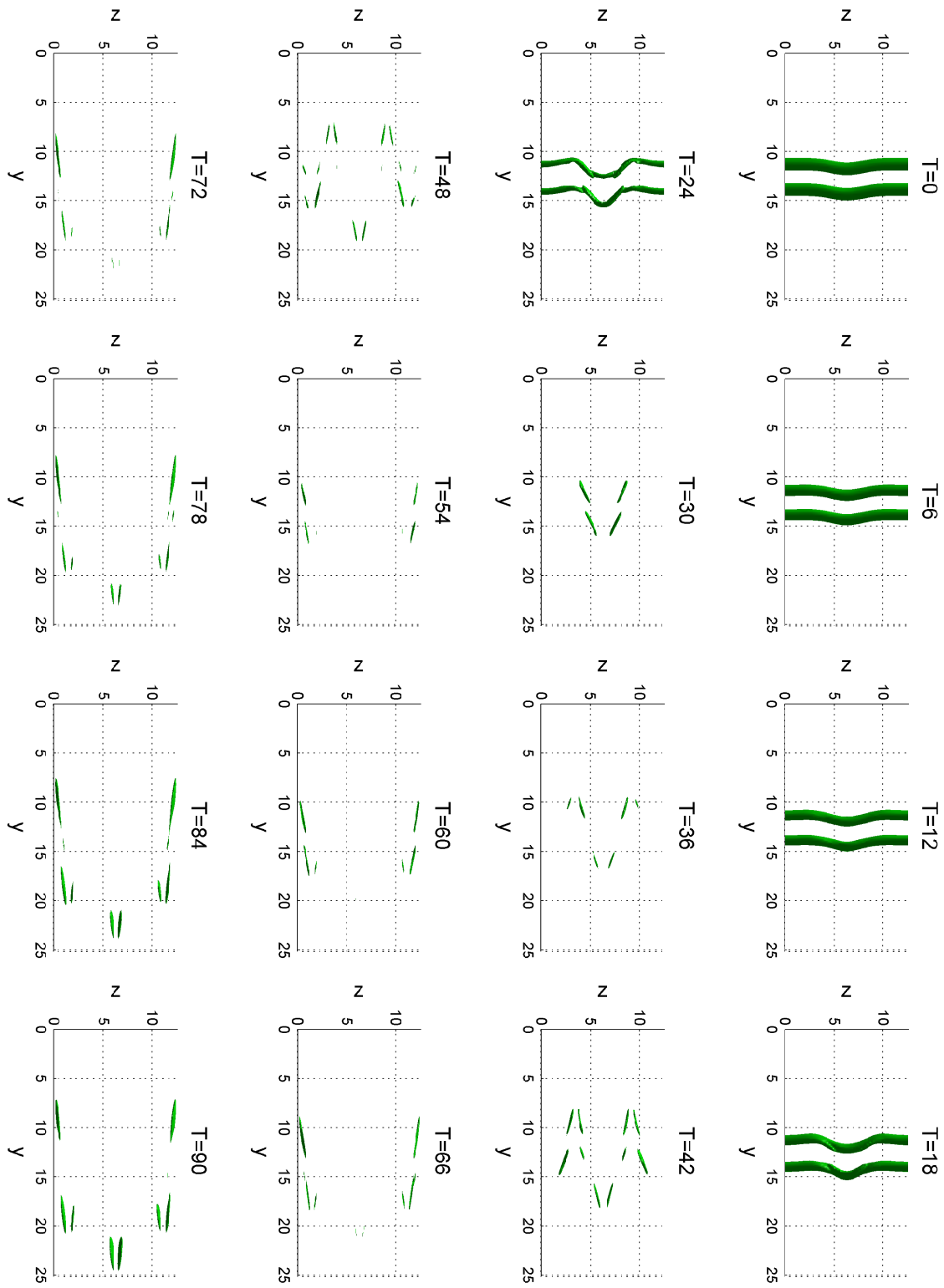

Figure 4.12: Evolution of the pair of vortex columns, in the $y-z$ plane, with the perturbation applied coplanar perpendicular to the direction of travel. Enstrophy isosurface value taken as $0.5 \cdot \max_{\boldsymbol{x} \in \mathscr{D}} (\boldsymbol{Z})$.

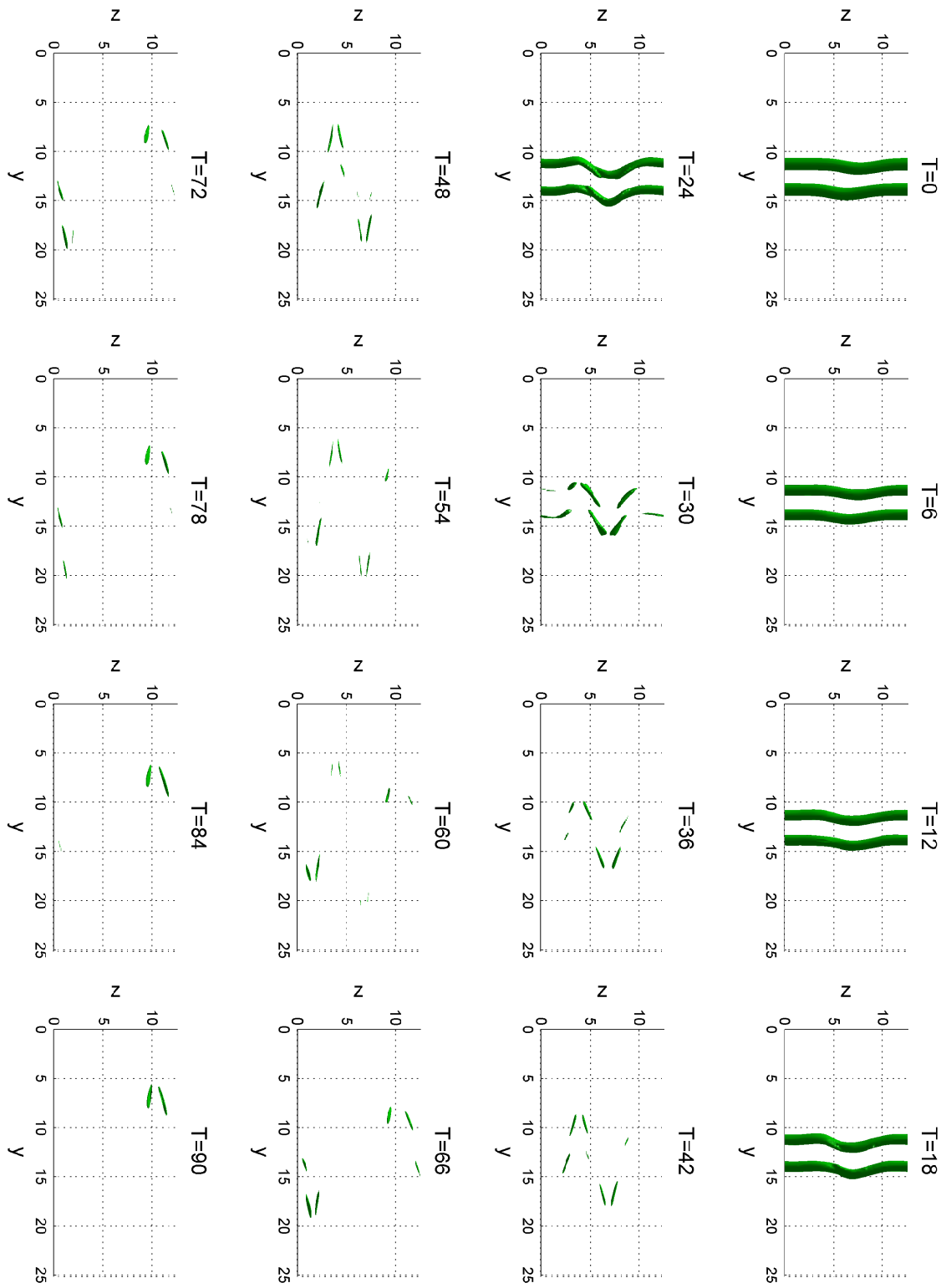

Figure 4.13: Evolution of the pair of vortex columns, in the $y-z$ plane, with the perturbation applied offset perpendicular to the direction of travel. Enstrophy isosurface value taken as $0.5 \cdot \max_{\boldsymbol{x} \in \mathscr{D}} (\boldsymbol{Z})$.

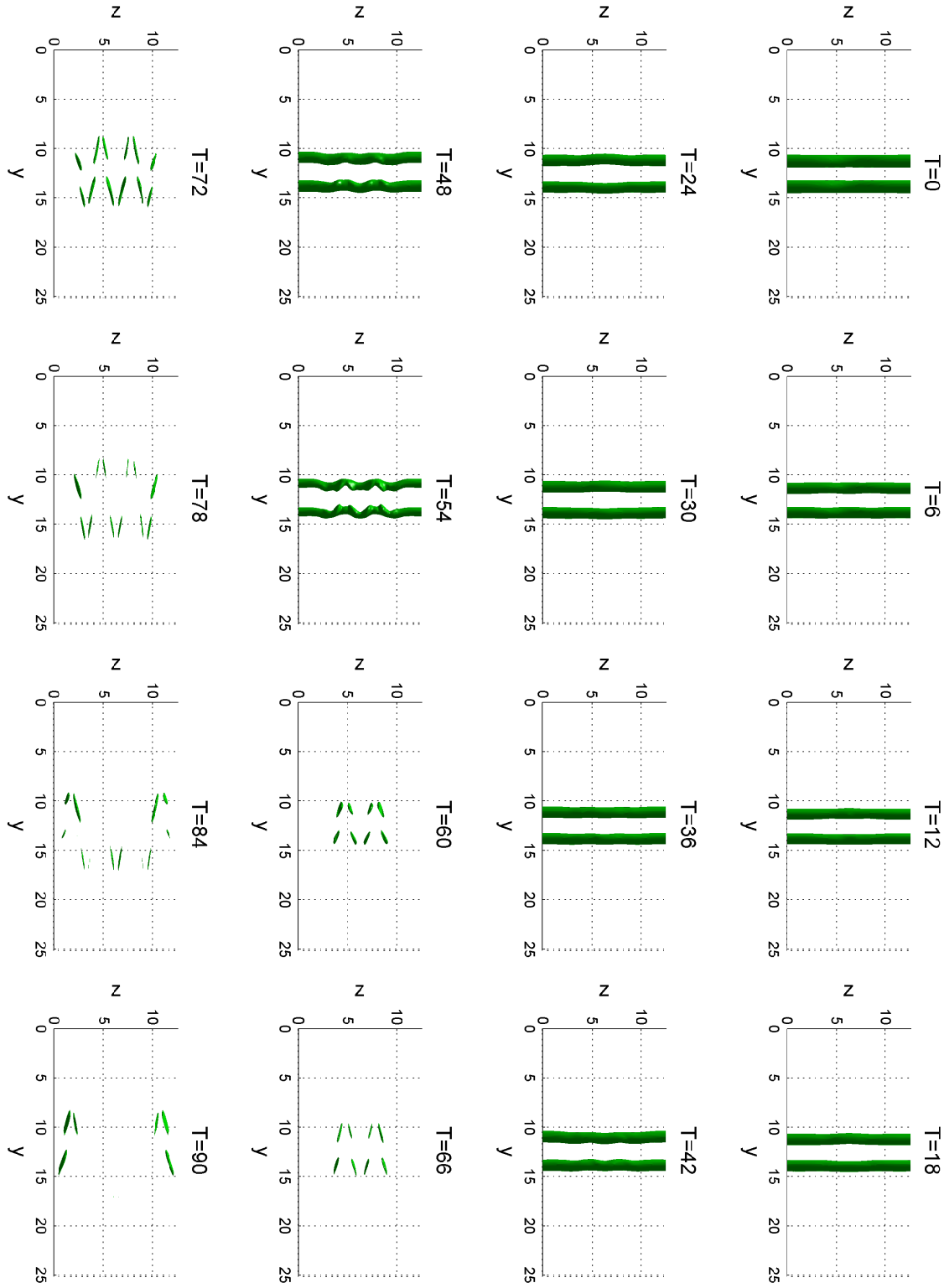

Figure 4.14: Evolution of the pair of vortex columns, in the $y-z$ plane, with the perturbation applied coplanar in the direction of travel. Enstrophy isosurface value taken as $0.5 \cdot \max_{\boldsymbol{x} \in \mathscr{D}} (\boldsymbol{Z})$.

Since the four simulations of two counter rotating vortices with various perturbations applied all show the onset and development of the zigzag instability, we continue by identifying the specific initial profile which leads to the fastest growth of the instability. In order to determine this we consider the total growth in enstrophy with time. The sum total enstrophy along with its three components in the x, y and z direction for each of the four initial profiles are shown in Fig. 4.15. Each of the four profiles show, at some point in time, exponential growth in total enstrophy (green line) which reaches a peak and then decays away exponentially. The time at which this peak in total enstrophy occurs differs for each of the profiles,

Simulation	Time of peak enstrophy
OPa	36
CPe	52
OPe	50
CPa	76

though it is clear that the initial condition which had offset perturbations in the direction of vortex travel enters the exponentially enstrophy growth and subsequently reaches peak enstrophy the quickest of any of the four profiles. This simulation, OPa, reaches its peak total enstrophy value of 0.35 at $t = 36$ which is 2.12 times the initial total enstrophy of the system. Simulation CPe, reaches approximately the same total enstrophy value however takes much longer to attain it, $t = 52$. Profiles OPe and CPa do not reach a peak total enstrophy as high as OPa and their respective peaks occur much later in time.

Our aim for this section was to identify an initial profile for the two counter rotating vortex columns which would become more unstable to the zigzag instability that just a sinusoidal perturbation applied to the vortex columns. We have identified profiles that are more unstable than this, OPa and CPe, and of these profiles initialising the vortex columns with perturbations applied locally within the columns, in the direction of travel and also offset from each other in the horizontal plane was

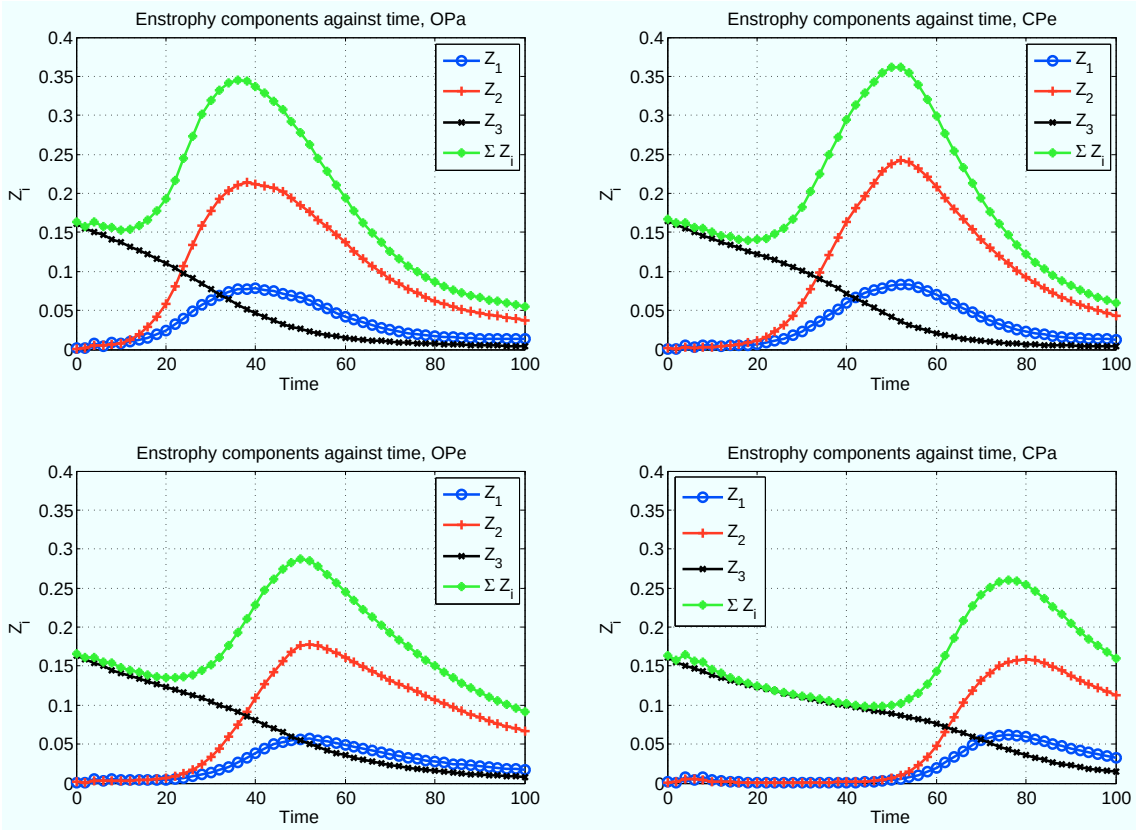

Figure 4.15: Change through time of the three components of enstrophy and their sum for the four new initial profiles.

found to become unstable the soonest. Given this finding, from now onward we consider only this initial profile, the simulation of which we study in more detail in the next section.

4.5 Most Unstable Initial Condition

Having established an initial profile that is more unstable than the sinusoidal profile we wish to understand more about the zigzag instability, what contributes to the production of enstrophy and implications for the cascade of energy.

4.5.1 Evolution of Vortex Columns and Growth

Figure 4.17 shows the profiles of vorticity through the plane $z = 4\pi$ at $t = 0$. Figures 4.18 and 4.19 are similar to Figs. 4.7 and 4.11, but with frames shown more frequently. We see that up until $t = 8$ the stretching of the vortex column is minimal, this is due to the minimal growth in enstrophy during this phase. In Fig. 4.15 we see that during this period, for the OPa figure, the total enstrophy decays slightly as Z_z decays and $Z_{x,y}$ both grow slightly. From $t = 10$ the growth of Z_y increases exponentially, which we also see in the subsequent frames of Fig. 4.19, the vortex columns rapidly stretch out in the y direction, flattening into layers. These layers stretch out mostly in the y direction, but do also spread in the x direction (as can be noted in the $t = 18$ frame of Fig. 4.18). This explains the small growth seen in the x component of enstrophy which follows a similar growth and decay profile as Z_y. The vortex 'sheets' that develop due to the zigzag instability confine themselves to discrete horizontal layers, hence we see no growth in the vertical enstrophy component, Z_z which gradually decays. This decay is slightly more rapid during the period in which the horizontal components of enstrophy grow exponentially quickly; the Z_z enstrophy decays at a continued slowing rate soon after $Z_{x,y}$ attain their respective peak values.

The growth of the zigzag instability for this profile can be measured by computing the Euclidean distance between the point which is the in the corner of the bend in the vortex column furthest away from the main vortex body and the centre of the vortex on the same $x - y$ plane as this corner point. Figure 4.16 plots these Euclidean distances against time. The rate of growth of the zigzag instability can then be calculated as the derivative of these Euclidean distances. Theoretical work by Billant et al. (2010, [24]) derived the maximum rate of growth for the zigzag instability as

$$\frac{\Gamma}{2\pi a^2} \tag{4.2}$$

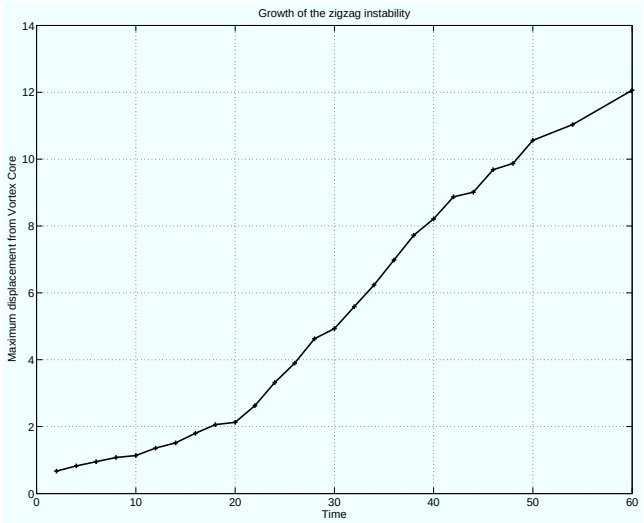

Figure 4.16: Growth of the zigzag instability measured by furthest distance away from vortex core.

in the case of two vortex columns with the velocity field initially perturbed sinusoidally ([3], section 2). In the case of this initial condition, OPa, this theoretical maximum growth rate evaluates to

$$\frac{10.06}{2\pi \times 2.34^2} = 0.29$$

However, computing the observed maximum growth rate of the OPa initial condition gives a value of 0.372 at $t = 34$, a 27% increase over the expected theortical value. This higher value for the maximum growth rate of the zigzag instability that we have obtained shows that considering a wider range of possible vortex initial profiles that include offset pertubrations, results in a simulation rapidly unstable to the zigzag instability. In order for one to derive an expression for the theoretical maximum growth rate of the zigzag instabiltiy an extension of the initial condition Billant and Chomaz chose is required.

The growth in total enstrophy can be considered alternatively based on the components that contribute positively to enstrophy, vortex stretching and baroclinic production of vorticity. These two components are defined in the right hand side of

the enstrophy equation (2.9).

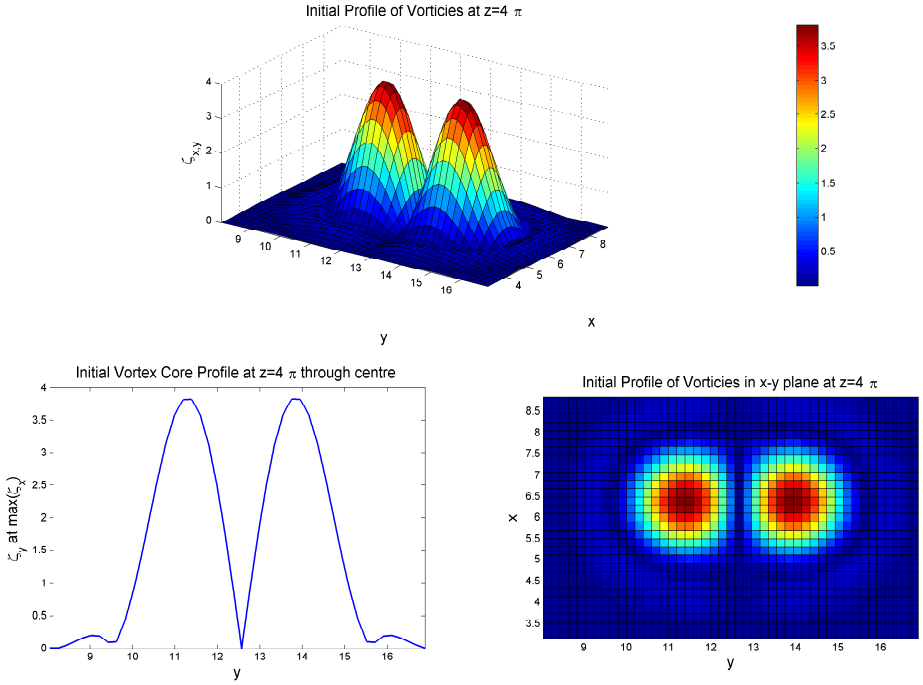

Figure 4.17: Depictions of the enstrophy profiles of the initial vortex columns. The core radii, $r = 1.315$, the separation of the two cores, $a = 2.338$, and the vortex circulations are $\Gamma_{1,2} = \pm 10.055$.

4.5.2 Production of Enstrophy

The rate of change of total enstrophy, $\partial_t \boldsymbol{Z}$, was defined previously by the enstrophy equation (2.9), in which first two terms on the right of (2.9) correspond to production of enstrophy due to vortex stretching and baroclinic production respectively, hence to understand the growth in enstrophy seen in Fig. 4.15 one would wish to understand the nature of these two terms of enstrophy production within our current simulation of study. Figure 4.20 shows isosurfaces of enstrophy along with isosurfaces of enstrophy production, vortex stretching in cyan colour and baroclinic production coloured in magenta. Initially, at $t = 2$, we see small surfaces of vortex stretching but no baroclinic vorticity production. The surface of vortex stretching in the left column appears at the first bend, around $z = 8$, in the vortex column

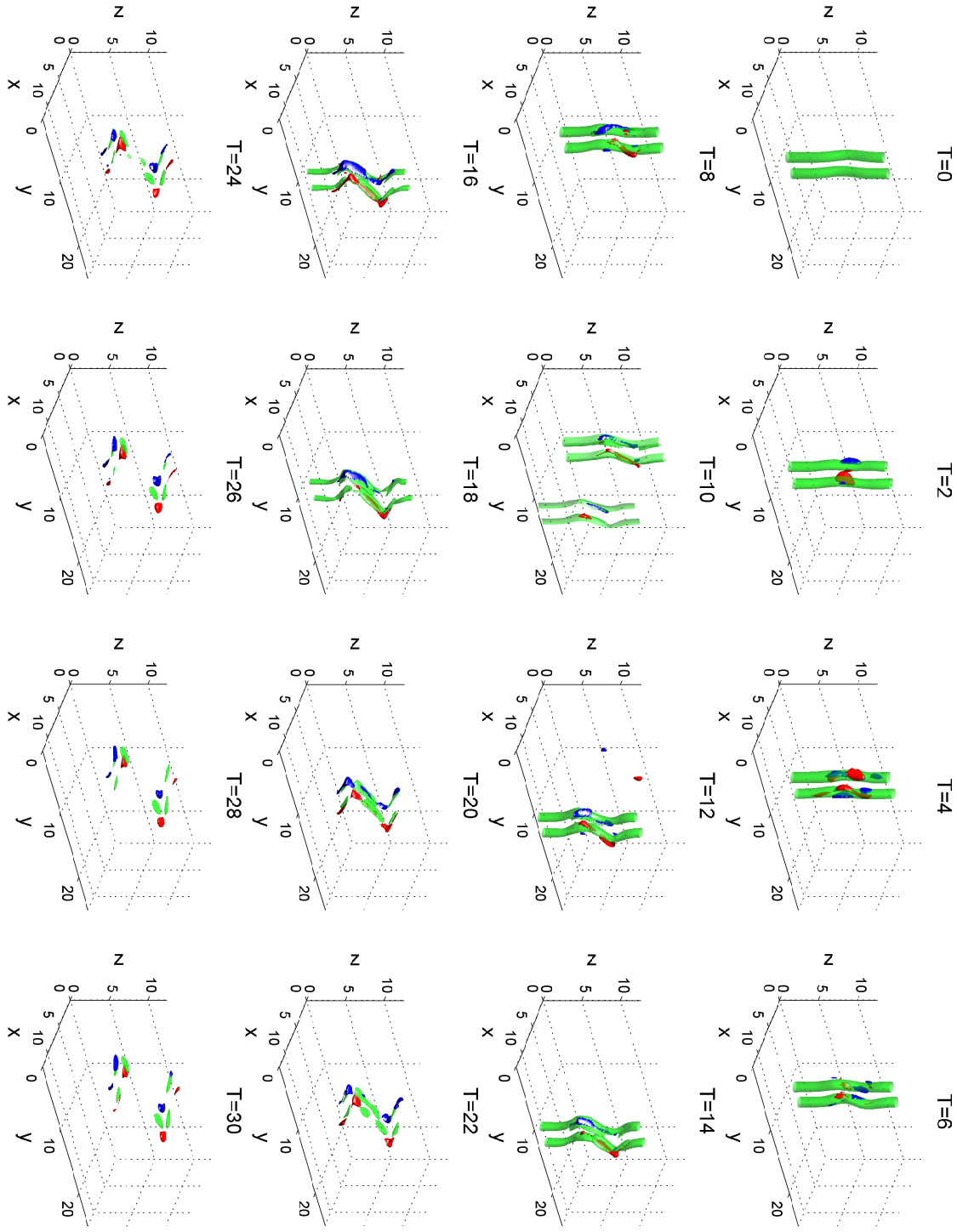

Figure 4.18: Early time evolution of the pair of vortex columns which began with an offset perturbation parallel to the direction of travel. Red and blue isosurfaces of positive and negative potential vorticity, $\pm 0.55 \cdot \max_{\boldsymbol{x} \in \mathscr{D}} (PV)$. Images shown more frequently than in Fig. 4.7.

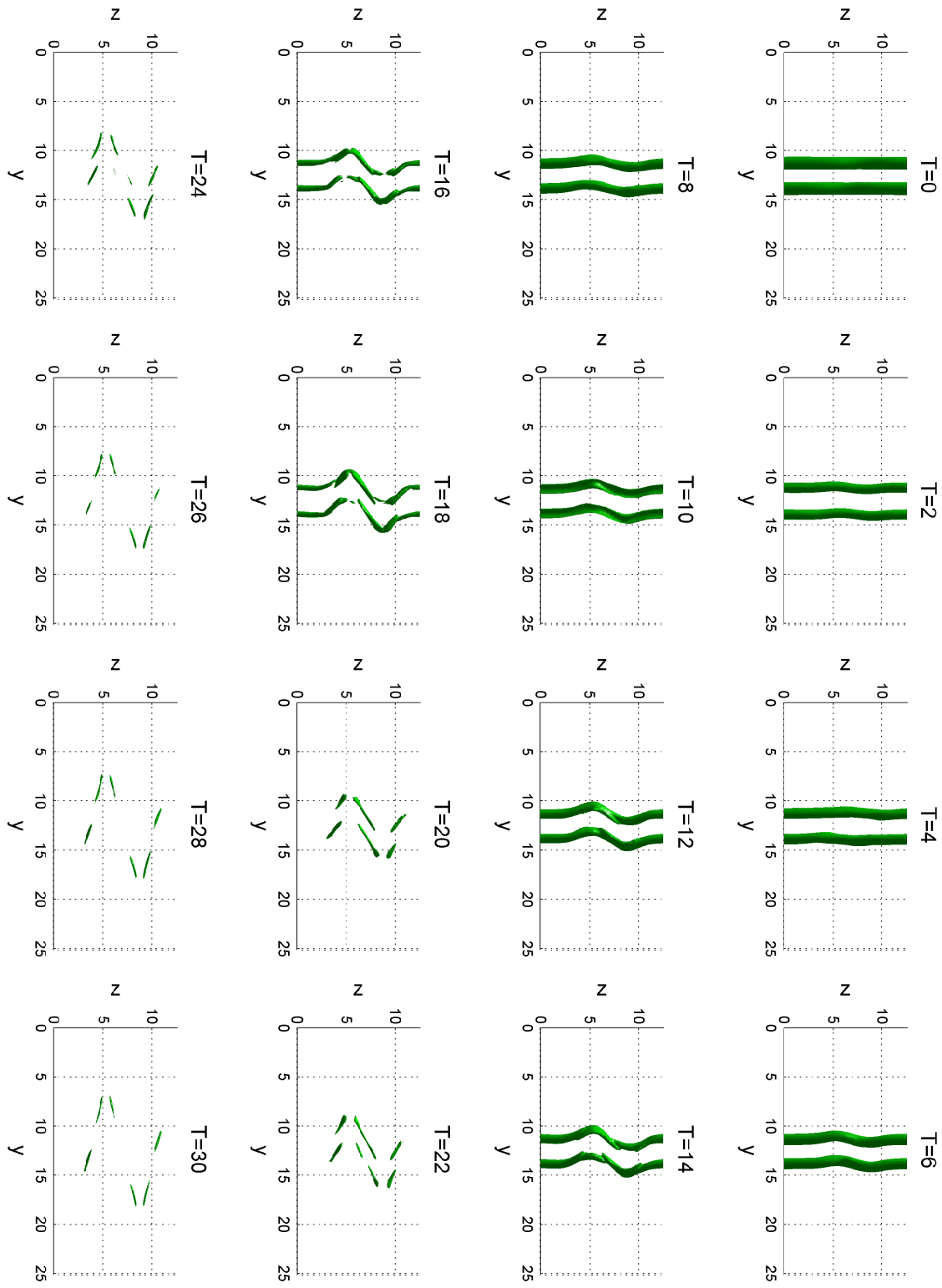

Figure 4.19: Early time evolution of the pair of vortex columns, in the $y-z$ plane, with the perturbation applied offset in the direction of travel. Images shown more frequently than in Fig. 4.11. Enstrophy isosurface value taken as $0.5 \cdot \max_{\boldsymbol{x}\in\mathscr{D}}(\boldsymbol{Z})$.

(when looking from the top of the column to the bottom) and in the right column at the second bend, around $z = 6$, in the vortex column. It is this initial stretching of the top part of the left vortex column in the increasing y direction and stretching of the centre of the right column in the decreasing y direction that causes the vortex columns to begin bending and forming the initial stages of zigzags. As time progresses we start to see additional enstrophy production due to baroclinic production, first visible in the $t = 8$ frame. In this same frame we also see greatly increased surfaces of vortex stretching, which continues to be strong at the bends of the vortex columns. However, we additionally see that the left vortex column is also stretching in the area between the two bends at approximately $z = 8$ and $z = 5$. These are the surfaces that eventually form the flat horizontally decoupled layers we have seen in the latter frames of Fig. 4.7. The isosurfaces of baroclinic vorticity production in the $t = 8$ frame also appear at the bends of the vortex columns, however whereas the isosurfaces of vortex stretching align themselves with the top surfaces of the vortex columns (when considering in the view presented in the figure), baroclinic production occurs at the front and back edges of the vortex column. This alignment of enstrophy production terms is clearer in the $t = 14$ and $t = 20$ frames. By $t = 20$ we see that the isosurfaces of vortex stretching have extended well beyond the initial diameter of the vortex column, in essence the enstrophy is beginning to be pulled out into flat sheets. At $t = 30$, which is just prior to the peak in enstrophy attained (see Fig. 4.15), we note large surfaces of vortex stretching and baroclinic production in the same orientations as observed in prior frames. These vortex stretching terms continue to stretch and decouple the vortex into horizontal layers, with vortex stretching terms pulling enstrophy in the y direction and baroclinic production in the x direction. A common theme among all the frames in Fig. 4.20 is that isosurfaces of vortex stretching are much larger than those of baroclinic production, this implies that enstrophy production is largely driven by vortex stretching over baroclinic production. The dominance of the stretching term over the baroclinic was

also observed by Deloncle et al. [3], however in the simulation carried out by the authors of [3] they observed no enstrophy production due to the baroclinic term. This provides a further possibility as to why the initial condition presented here (OPa) has faster growth in total enstrophy.

Figures 4.21 and 4.22 depict isosurfaces similar to Fig. 4.20 but with vortex stretching surfaces and baroclinic production surfaces shown in separate frames along with an additional frame of their sum.

The largest contributor to growth in total enstrophy for this initial condition is the y component of enstrophy as seen in Fig. 4.15 with x component of enstrophy contributing a small amount. This is consistent with the observation that vortex stretching is pulling in the y direction with baroclinic enstrophy growth in the x direction and with total enstrophy begin largely driven by the vortex stretching component of 2.9. The concept of vortex stretching and baroclinic production acting primarily in the y and x directions respectively is more clearly illustrated in Figs. 4.23 and 4.25.

Figure 4.23 shows the usual enstrophy isosurfaces of the vortex columns along with vectors of vortex stretching, defined as [26]

$$(\boldsymbol{\zeta} \cdot \nabla)\, \boldsymbol{u} \tag{4.3}$$

where S_{ij} is the strain tensor. In general, we note that the vectors of largest magnitude tend to point in the y direction as is consistent with the hypothesis that since vortex stretching is dominant over baroclinic production of enstrophy and total enstrophy growth is dominated by growth in Z_y over Z_x then the majority of vortex stretching occurs in the y direction. For $t = 20$, Fig. 4.24 is a zoomed in section of the corresponding frame from Fig. 4.23, in which the directions and magnitudes of the vectors are more clearly visible; $t = 20$ is during the phase of exponential enstrophy growth.

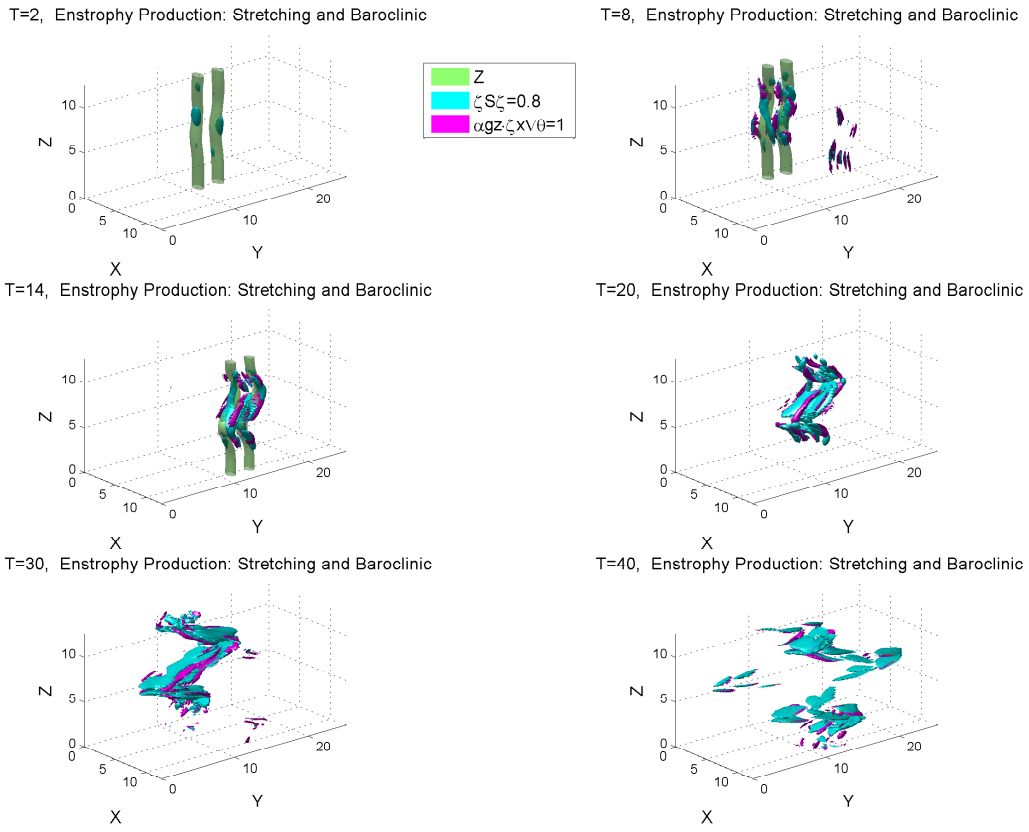

Figure 4.20: Isosurfaces of enstrophy, and enstrophy production through vortex stretching (cyan) and baroclinic production (magenta). Isovalues are; for enstrophy, $0.5 \cdot \max_{\boldsymbol{x} \in \mathscr{D}} (\boldsymbol{Z})$; for vortex stretching, 0.8 and for baroclinic production, 1.

We can also look at a similar set of production vectors for the baroclinic term, this is shown in Fig. 4.25. Baroclinic production vectors are defined as

$$\alpha g \hat{\boldsymbol{z}} \times \nabla \theta \tag{4.4}$$

where $\hat{\boldsymbol{z}}$ is the unit vector in the vertical and α the thermal expansion coefficient,

$$\alpha = \frac{1}{\rho} \frac{\partial \rho}{\partial \theta}$$

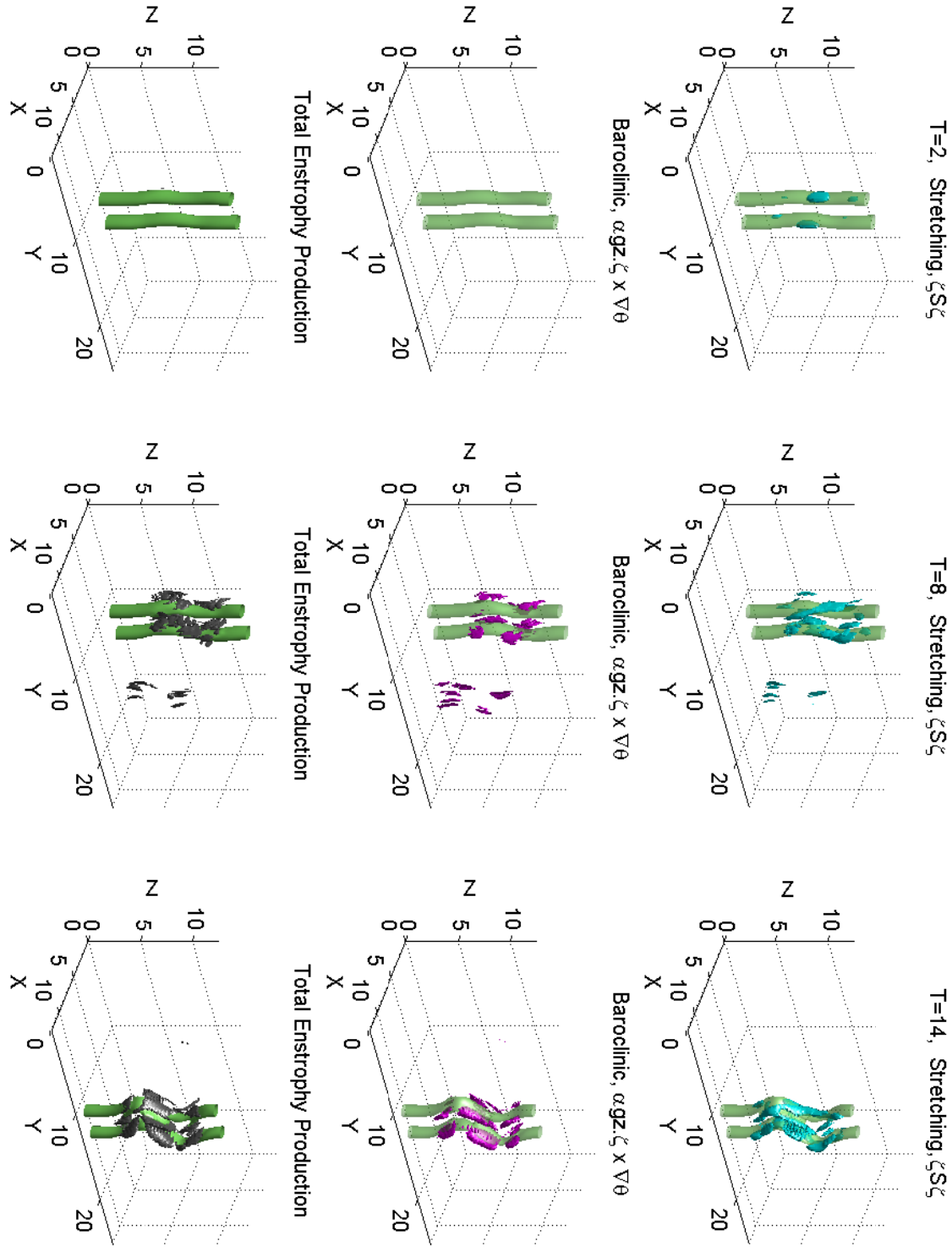

Figure 4.21: Three frames showing isosurfaces of vortex stretching (cyan), baroclinic production (magenta) and the total enstrophy production (black) at three different times. Isovalues are; for enstrophy, $0.5 \cdot \max_{\boldsymbol{x} \in \mathscr{D}} (\boldsymbol{Z})$; for vortex stretching, 0.8; for baroclinic production, 1 and for total enstrophy production, 2.

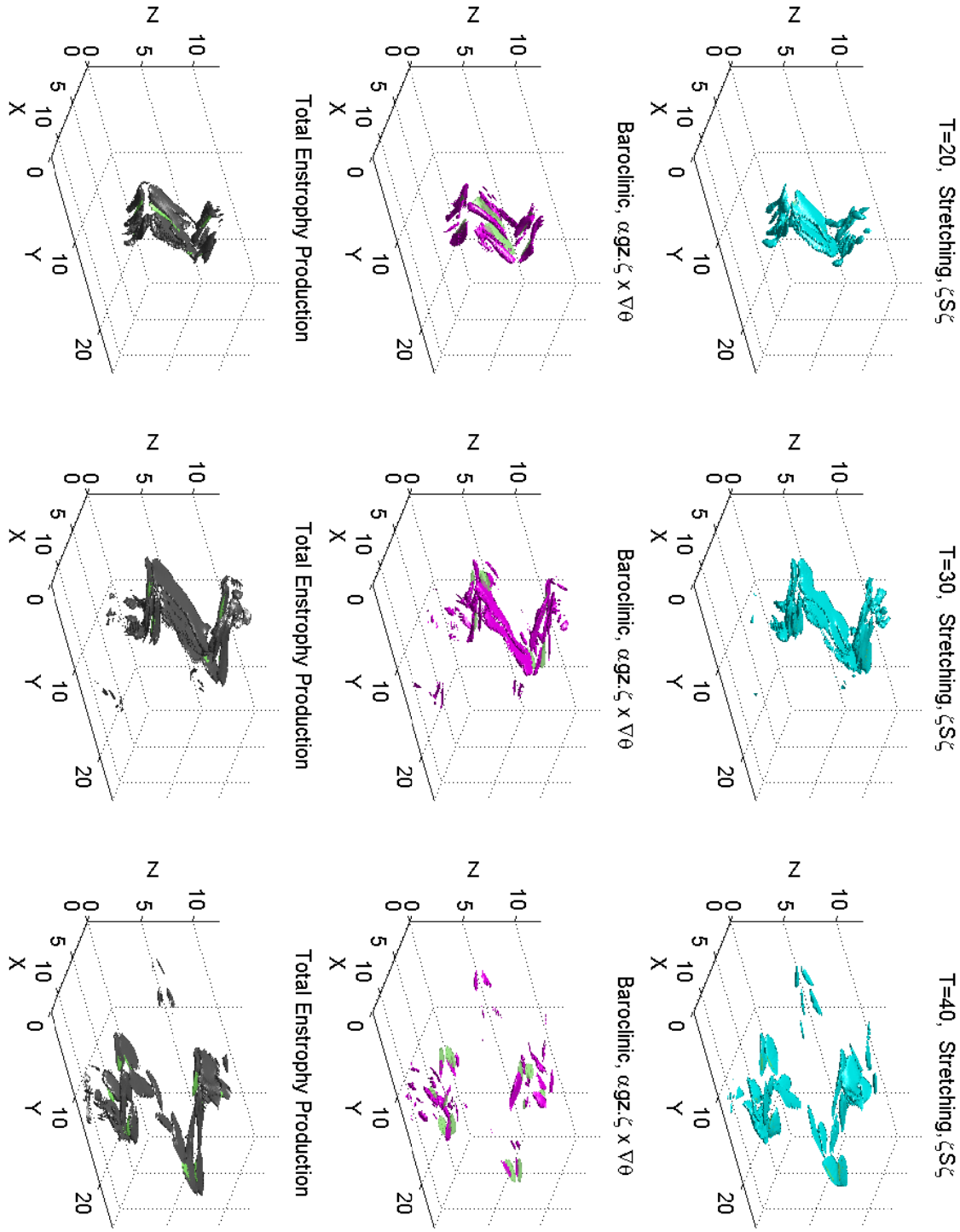

Figure 4.22: Three frames showing isosurfaces of vortex stretching (cyan), baroclinic production (magenta) and the total enstrophy production (black) at three different times. Isovalues for surfaces as in Fig. 4.21.

and is related to the Brunt Väisälä frequency, N, by

$$N^2 = \frac{-g}{\rho}\frac{\partial \rho}{\partial z} = \frac{-g}{\rho}\frac{\partial \rho}{\partial \theta}\frac{\partial \theta}{\partial z} = -g\alpha\frac{\partial \theta}{\partial z} \tag{4.5}$$

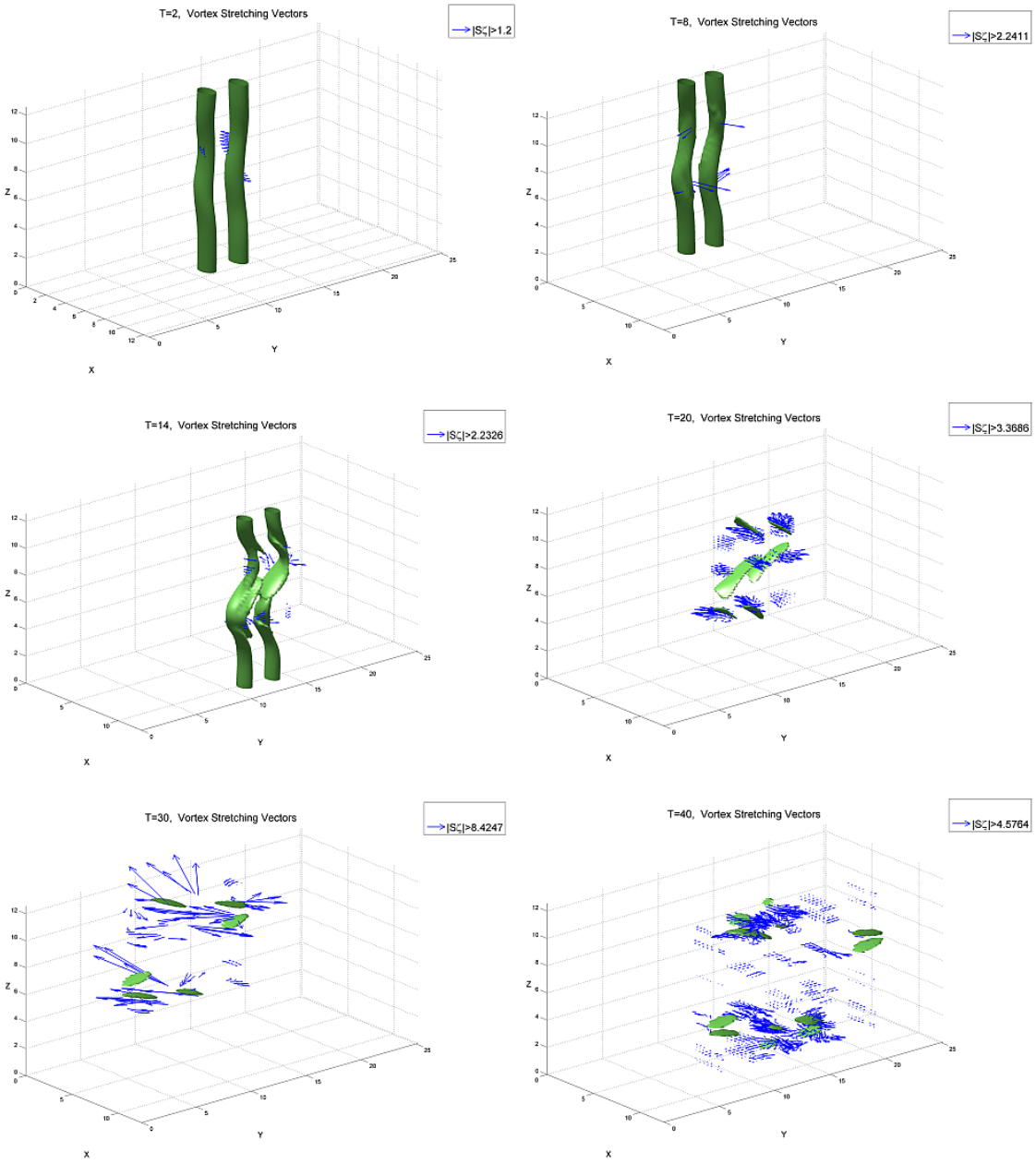

Figure 4.23: Enstrophy isosurfaces with vortex stretching vectors above the values given in the legends.

It is less clear to generalise the directions of baroclinic vectors to a single direction. Throughout the frames in Fig. 4.25 we notice that the vectors tend to follow the direction of vorticity. At $t = 14$ this is clearly depicted, the vector arrows of baroclinic production circle each of the two vortex columns, a zoomed in section at this time is shown in Fig. 4.26. An observation that also appears more clearly

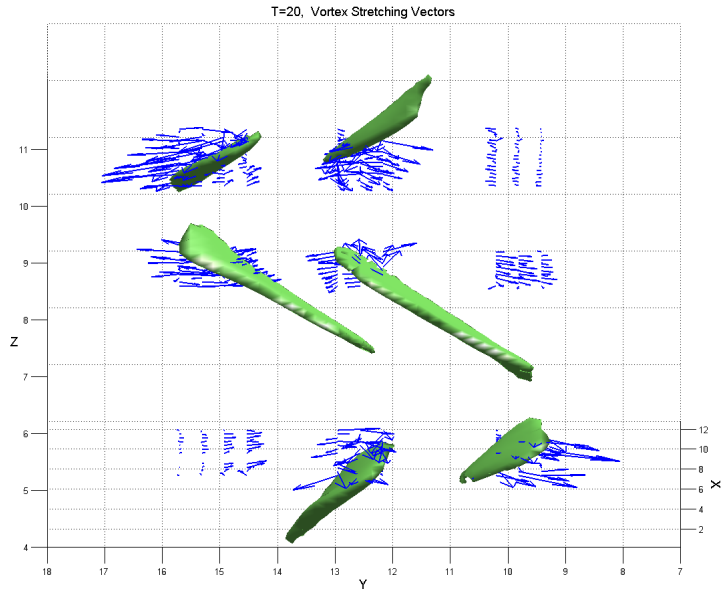

Figure 4.24: Enstrophy isosurfaces with vortex stretching vectors at $t = 20$, a zoomed in section.

in the zoomed in graphic, is that the largest magnitude vectors are mostly aligned with the x direction. Following the vectors around one of the vortex columns we see that in between the two columns the magnitudes of the vectors are large and are orientated in the x direction, then the arrows curve round the column and reduce in magnitude. At the point the arrows are furthest away from the column, they are of the smallest magnitude. As the arrows curve back around the vortex they increase in magnitude until they are aligned back in the x direction and are located between the vortex columns once more. This lends support to baroclinic enstrophy production, though smaller than enstrophy production due to vortex stretching, being the larger contributor to the growth in the enstrophy Z_x. Further to considering the vectors of enstrophy production terms around the vortex columns, we wish to understand the same within the columns.

By taking cross section through the vortex columns, in the $x - y$ plane, for various vertical points at multiple times we are able to better understand enstrophy production within the vortex cores. Figures 4.27 to 4.32 show these horizontal slices at times 2, 8, 14, 20, 30 and 40, with vortex stretching vectors in blue, baroclinic

production vectors in red and the sum of these as black vectors. At each time, cross sections are shown at 6 different z positions. We observe that the baroclinic vectors closely follow the lines of vorticity, within the vortex core, the vectors form tighter and tighter circles as they get closer to the vortex centre. This behaviour is most clearly observed in the $z = 7.6576$ slice at times $t = 14$ and $t = 20$ and also in Fig. 4.33 which is a zoomed in section of a $x - y$ plane at $t = 20$. Since the vectors of baroclinic production follow the vorticity, their directions are not in any one consistent direction (although vectors of largest magnitude are) this however is different for vortex stretching vectors. In any one z plane, typically vectors of vortex stretching align parallel to the same axis, though their direction in the increasing or decreasing direction may vary. For the vortex column whose centre is located at the greater y value of the two column centres, the vectors of vortex stretching point in the direction of increasing y; the opposite is true for the vortex column with centre at smaller y value, observable in Fig. 4.33.

We have seen so far the growth of the zigzag instability measured by the growth in total enstrophy of the system. This enstrophy we have broken down into its two components, vortex stretching and baroclinic production. Total enstrophy, as defined in (2.8), is the domain integral of vorticity squared and vorticity is the curl of velocity, $\boldsymbol{\zeta} = \nabla \times \boldsymbol{u}$. The velocity also arises in calculating the energy of the system, which we discuss next.

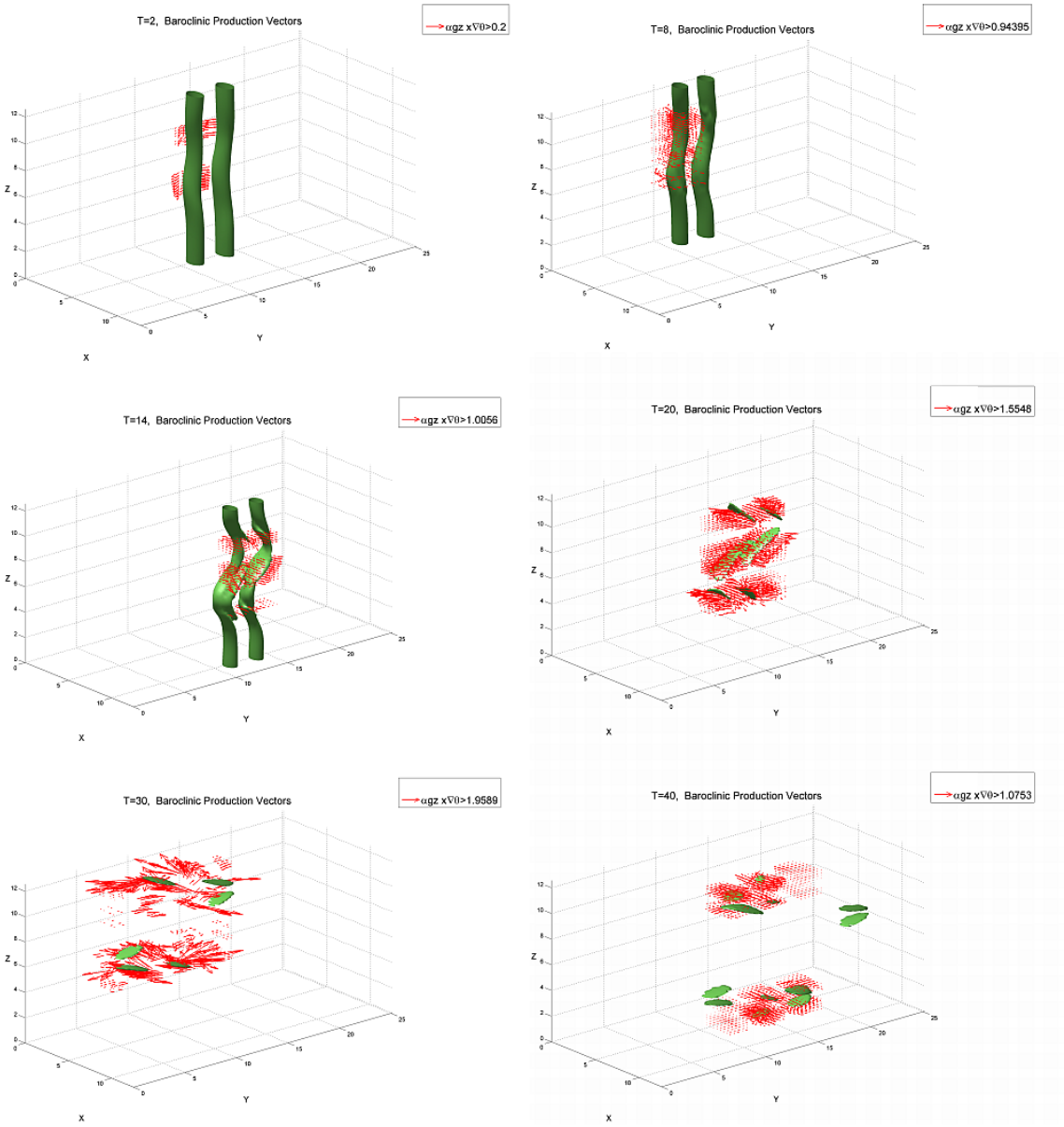

Figure 4.25: Enstrophy isosurfaces with baroclinic production vectors above the values given in the legends.

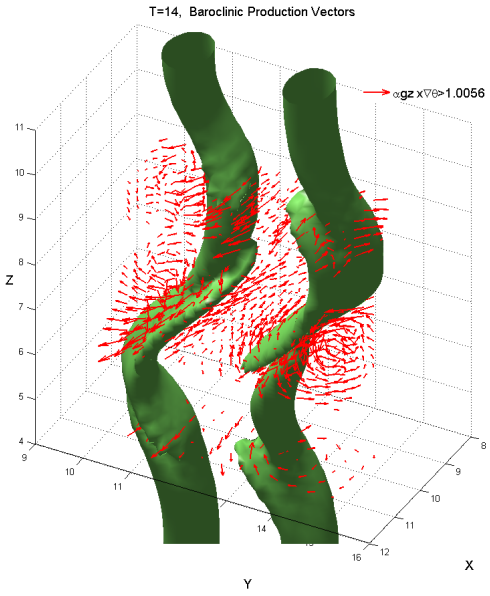

Figure 4.26: Enstrophy isosurfaces with baroclinic production vectors at $t = 14$, a zoomed in section.

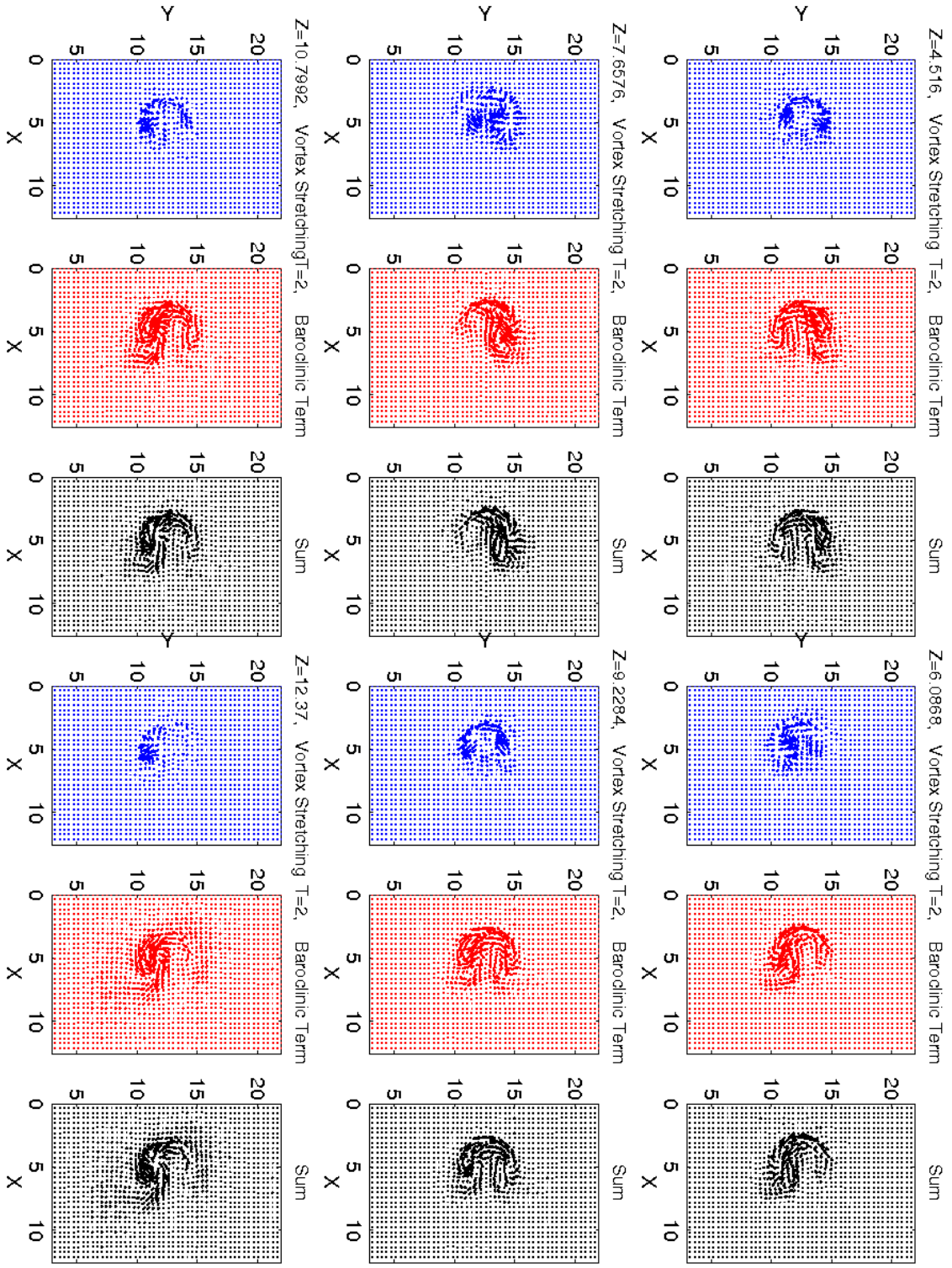

Figure 4.27: For $t = 2$, $y - x$ planes at 6 different z values of vortex stretching vectors (blue), baroclinic production vectors (red) and the sum of the two.

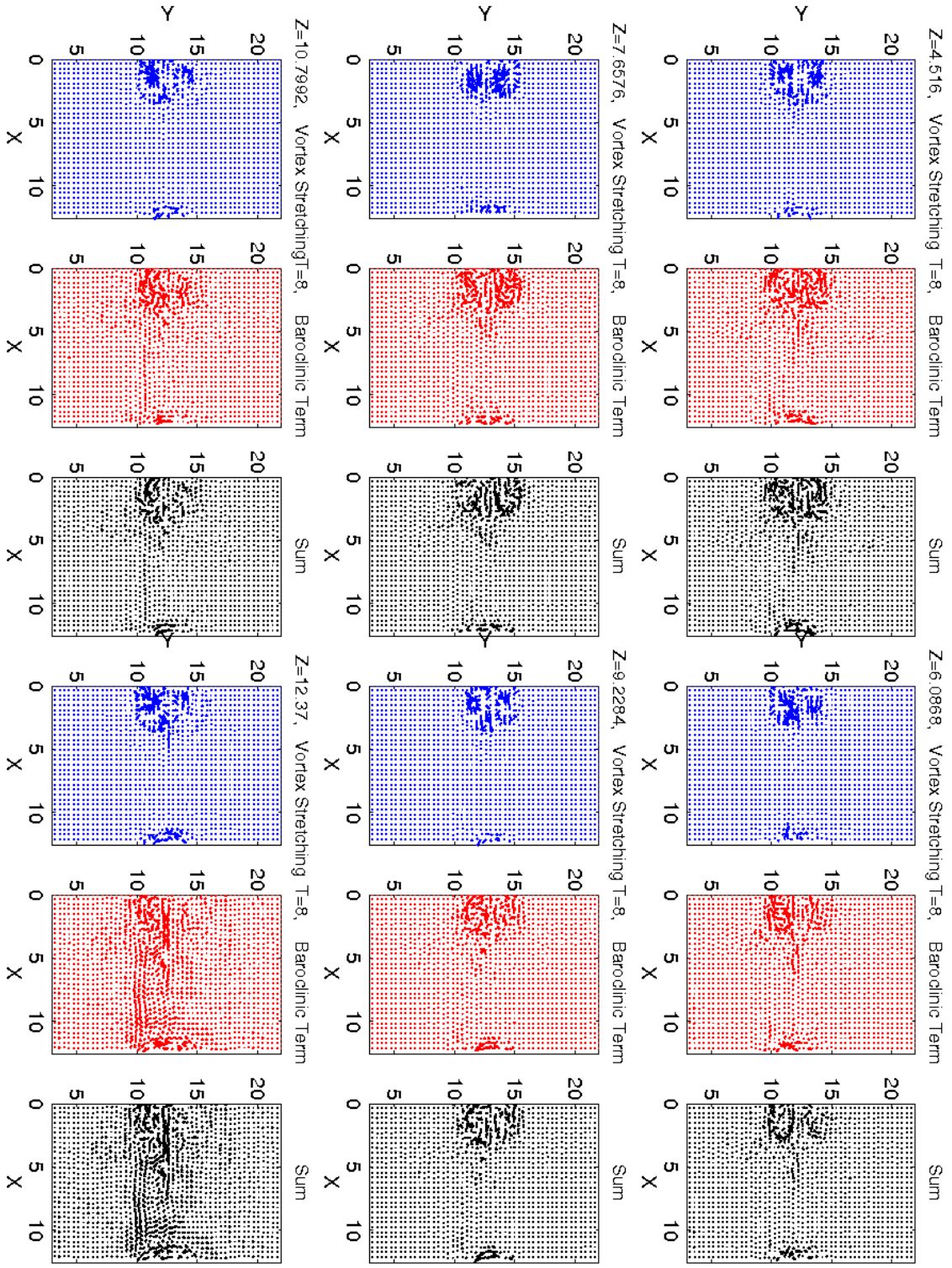

Figure 4.28: For $t = 8$, $y - x$ planes at 6 different z values of vortex stretching vectors (blue), baroclinic production vectors (red) and the sum of the two.

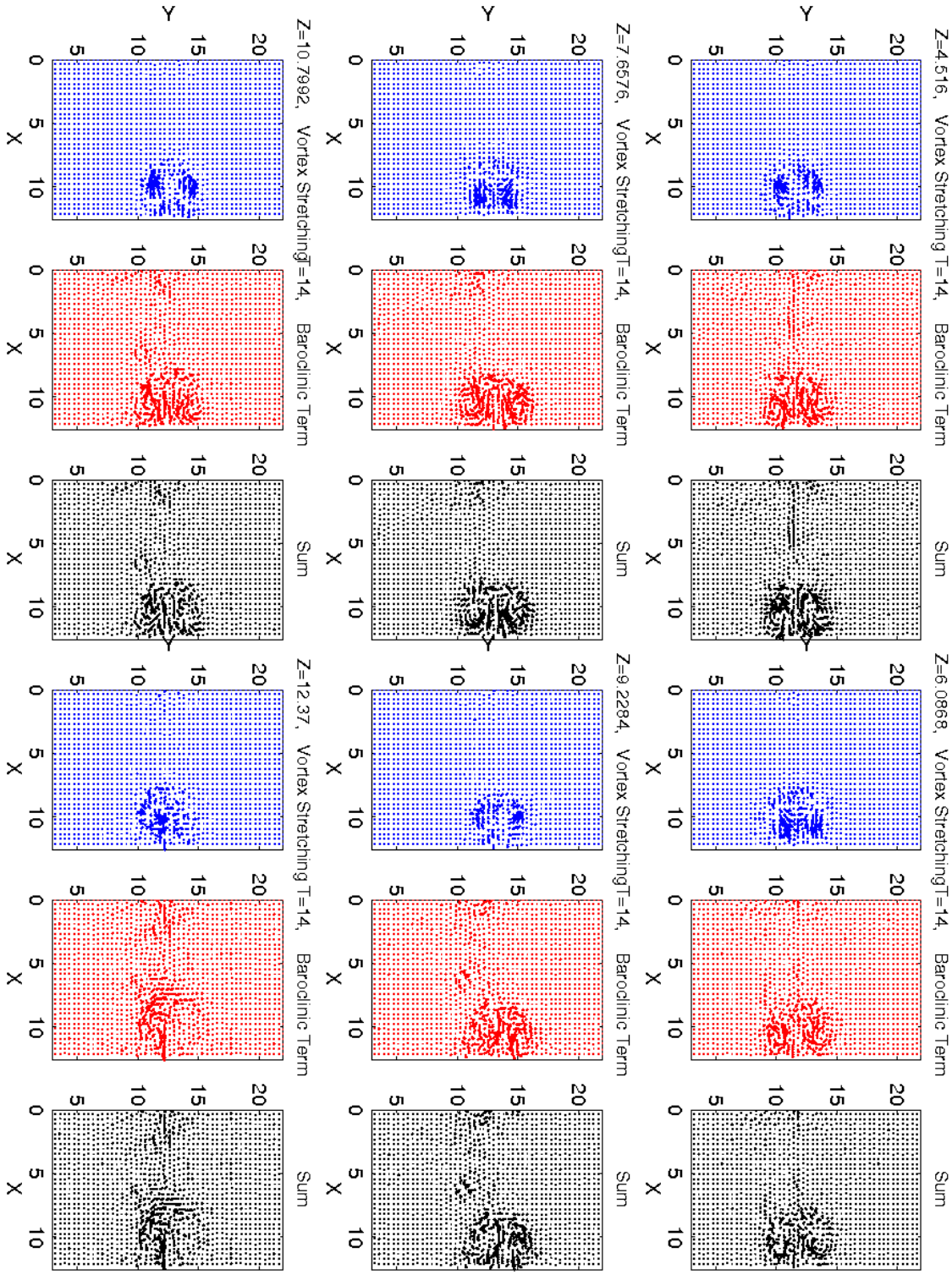

Figure 4.29: For $t = 14$, $y - x$ planes at 6 different z values of vortex stretching vectors (blue), baroclinic production vectors (red) and the sum of the two.

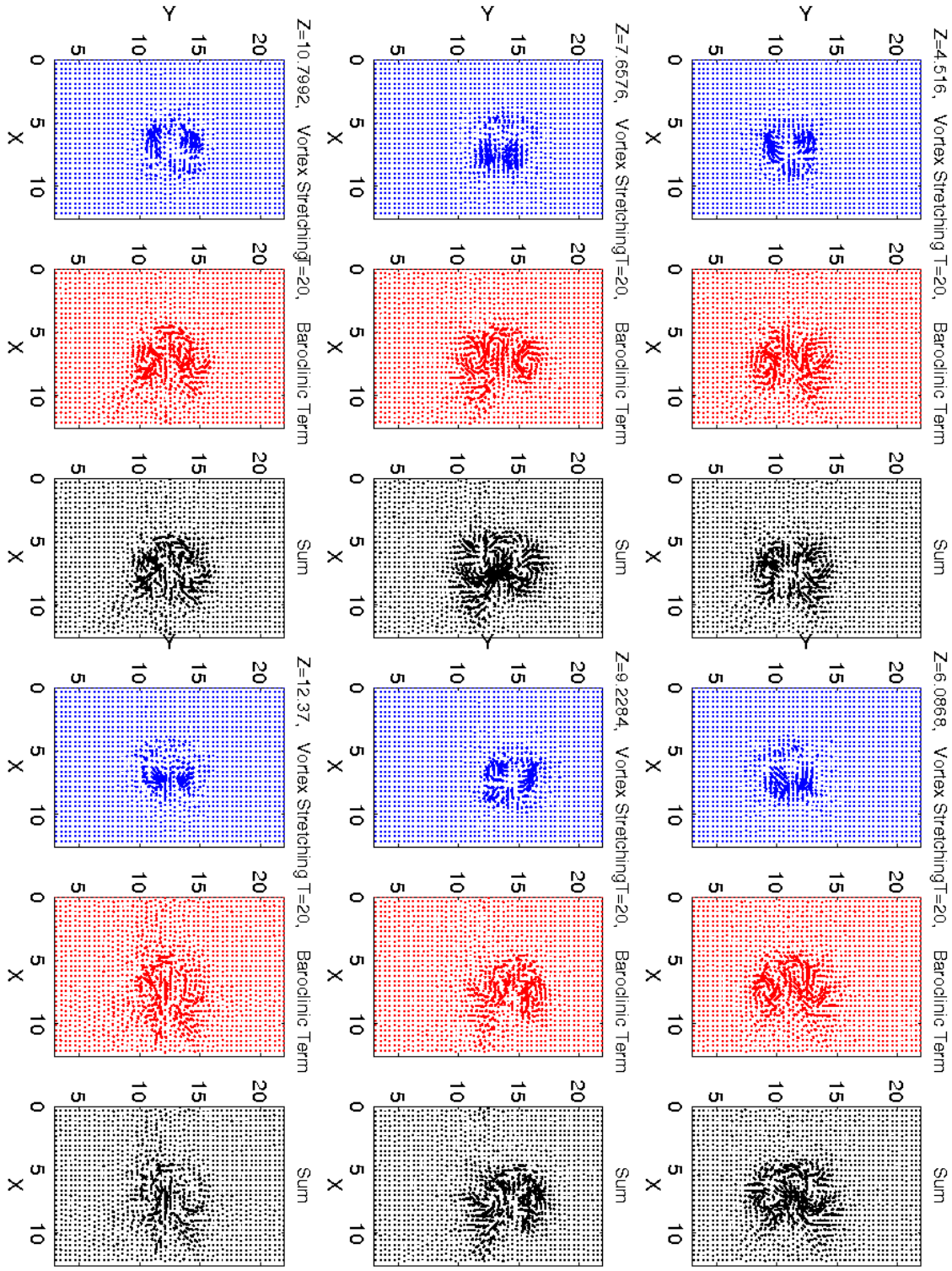

Figure 4.30: For $t = 20$, $y - x$ planes at 6 different z values of vortex stretching vectors (blue), baroclinic production vectors (red) and the sum of the two.

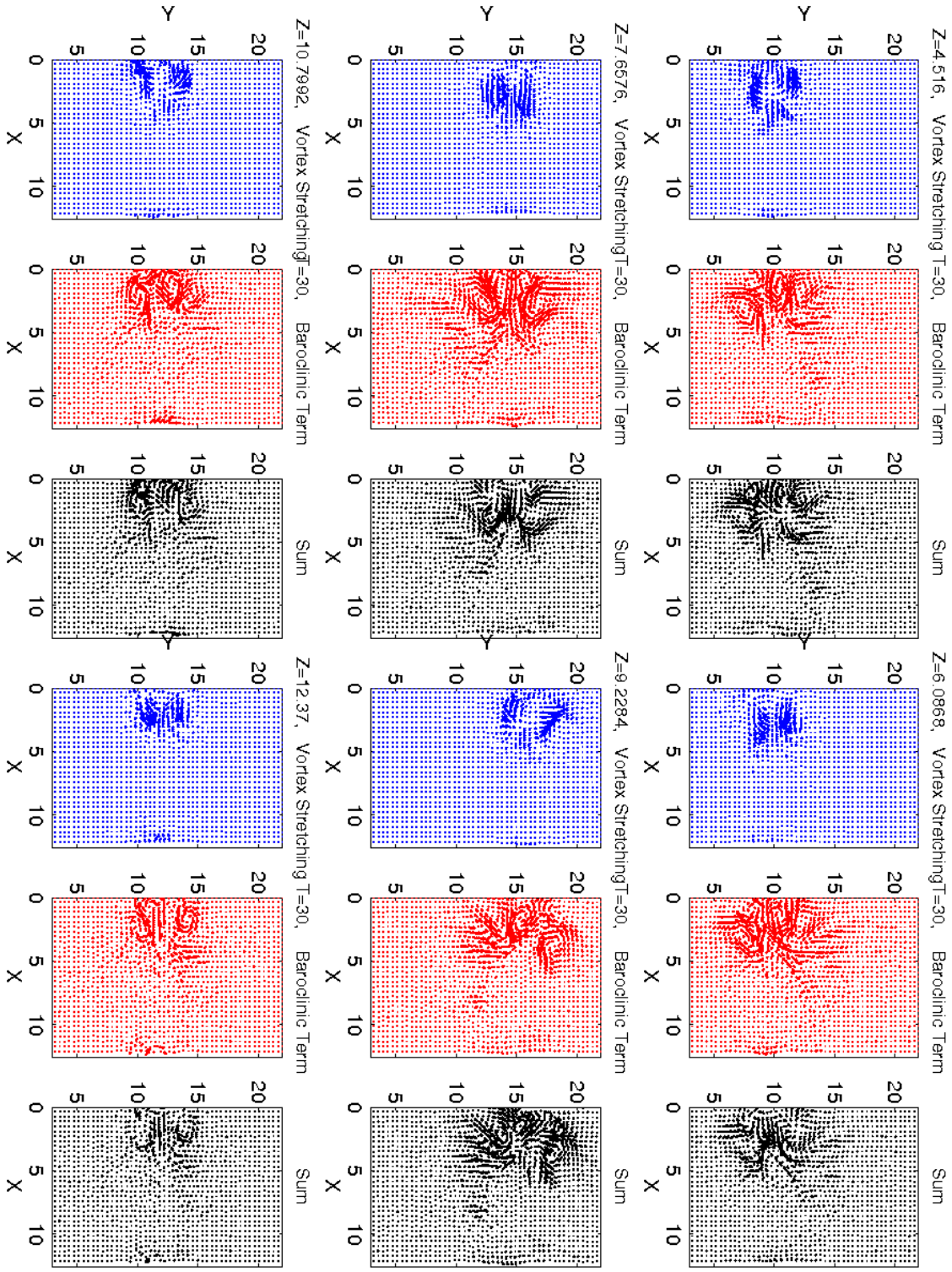

Figure 4.31: For $t = 30$, $y - x$ planes at 6 different z values of vortex stretching vectors (blue), baroclinic production vectors (red) and the sum of the two.

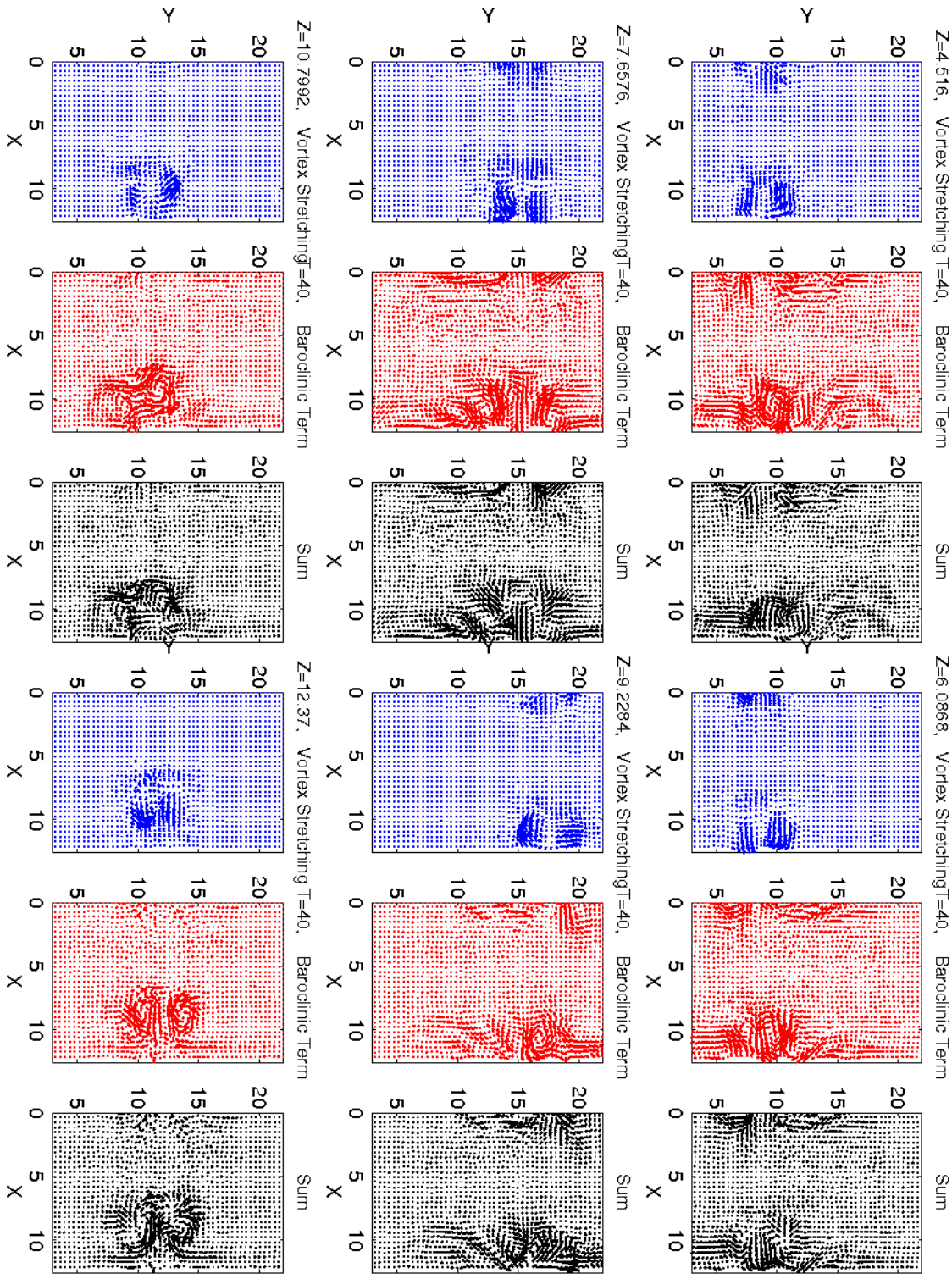

Figure 4.32: For $t = 40$, $y - x$ planes at 6 different z values of vortex stretching vectors (blue), baroclinic production vectors (red) and the sum of the two.

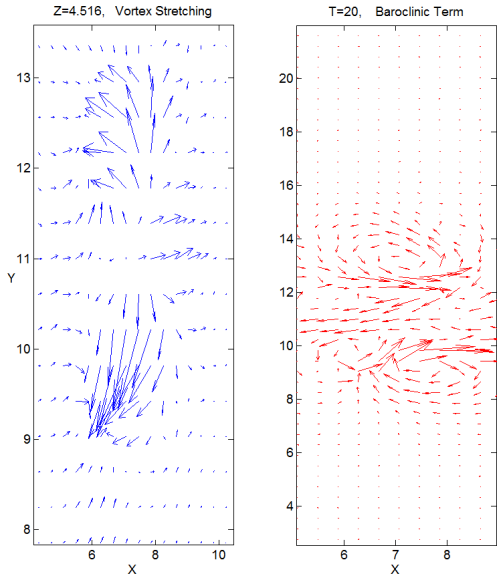

Figure 4.33: For $t = 20$, $y - x$ planes at $z = 4.5$ values of vortex stretching vectors and baroclinic production vectors.

4.5.3 Energies: Transfer and Spectra

We wish to further understand the consequence of the instability on the energy and its movement through the system in order to establish whether a cascade of energy exists and its nature. The three components of velocity; u, v and w, in the x, y and z directions respectively are shown against time in Fig. 4.35. We observe that horizontal velocity is dominant over vertical velocity (w has been multiplied by 100 in Fig. 4.35) and that the major component of the velocity at $t = 0$ is in the x direction. It is for this reason that the vortex columns propagate in the x direction rather than any other direction due to their mutual induction and opposite circulation. The velocity u decays at a fairly constant rate until $t = 50$ after which its rate of decay slows. Velocity in the y direction, v, decays gradually throughout with a slow rate of decay until $t = 30$ and a slight faster rate after that. Velocity component in the vertical is of the order of a hundred times less than the horizontal velocities as one would expect since due to the lack of vertical motions. These three components of velocity combined form the kinetic energy of the system. The final line on Fig. 4.35 is θ^2 (multiplied by 10), the square of the scalar. We note that it

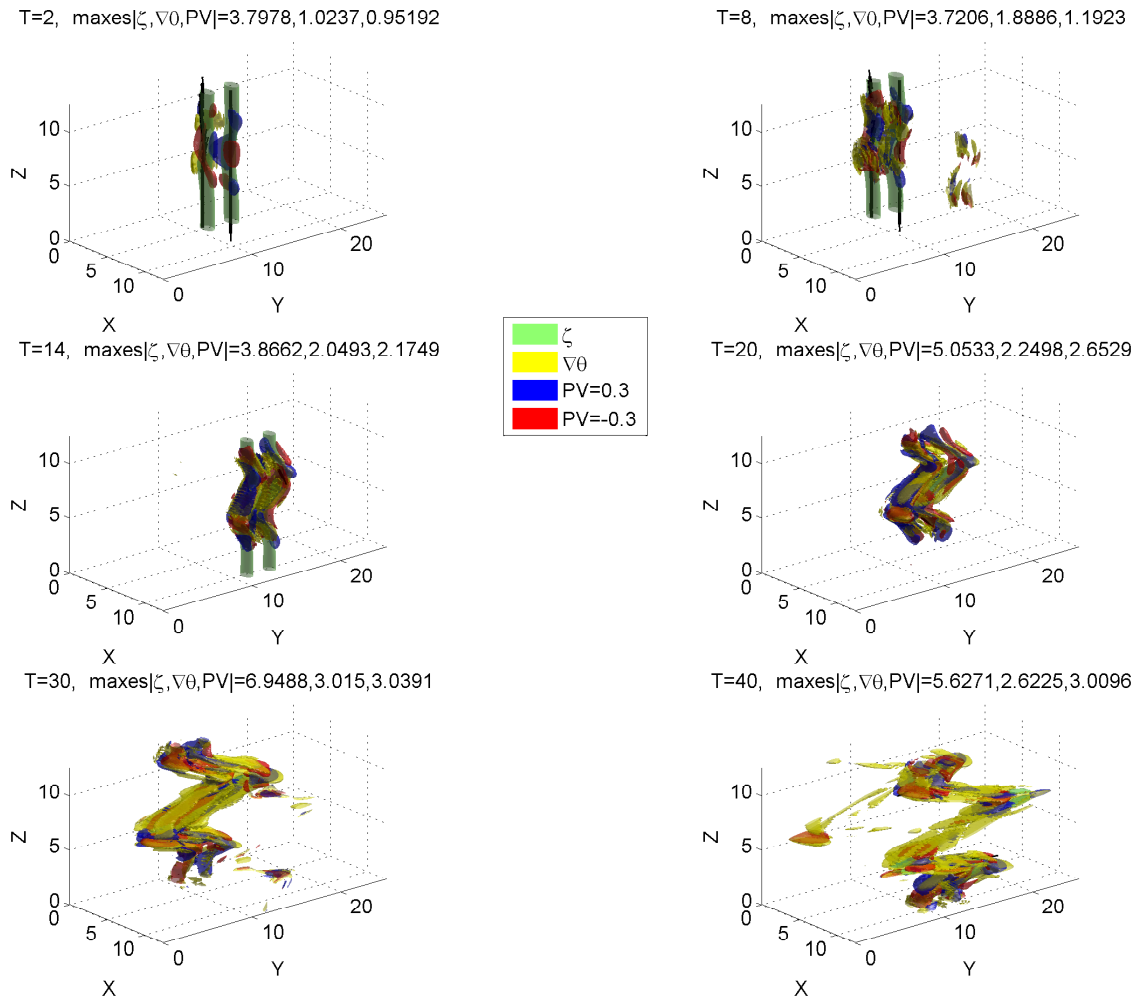

Figure 4.34: Isosurfaces of enstrophy, gradient of temperature, and potential vorticity. Isovalues are; for enstrophy, $0.5 \cdot \max_{\boldsymbol{x} \in \mathscr{D}} (\boldsymbol{Z})$; for $\nabla\theta$, 0.5 and for $PV \pm 0.3$.

follows a similar profile to that of total enstrophy, in that it grows rapidly to a peak, of 0.039/10, and then decays gradually. The square of the scalar is directly linked to the potential energy of the system, the potential energy is the product of the scalar and vertical distance. The implication being that energy is extracted from the mean temperature gradient and converted into kinetic energy and is contributing to creating the turbulent velocity fields.

The total energy is the sum of both the kinetic and potential energies within the

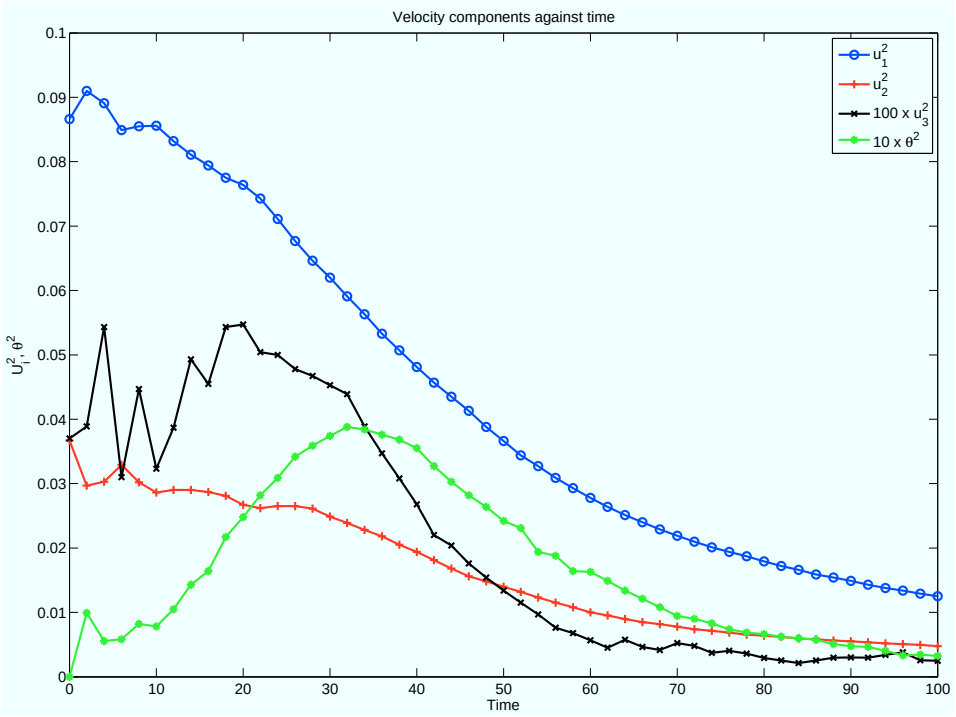

Figure 4.35: Change of x, y and z components of velocity and scalar squared through time.

system, that is

$$\begin{aligned} E &= E_k + E_p \\ &= \frac{1}{2}\int_{\mathscr{D}} \boldsymbol{u}^2 + z\theta d\mathscr{D} \end{aligned} \tag{4.6}$$

Figure 4.36 shows the evolution of these two components of energy, kinetic and potential, along with total enstrophy. The kinetic energy in the system decays with a similar profile as that of the greatest velocity u, as expected by the definition of kinetic energy and given observations from Fig. 4.35. That is, an initial period of slow decay followed by rapid decay between $t = 25$ and $t = 55$ and then continued slowing decay. The potential energy in the system at the start of the simulation is zero but grows quickly to a maximum level of 0.019 by $t = 32$, which is slightly earlier than the time of maximum total enstrophy. Profiles of kinetic and potential energy seen here can also be seen in simulations performed by Deloncle et al. [3, Fig. 2(a)].

However, we note in our simulation that kinetic energy reaches the stage of rapid decay at a time earlier than that seen in [3]. This provides further evidence that the initial condition presented here is more unstable than that presented in [3] since the energy in the system will rapidly decay as vorticity dissipates due to viscosity and smaller vortices that are produced by the zigzag instability will dissipate quicker than large stable vortex columns. The potential energy profile, and also its scale in comparison to kinetic energy observed in Fig. 4.36 is also seen in the same figure in [3].

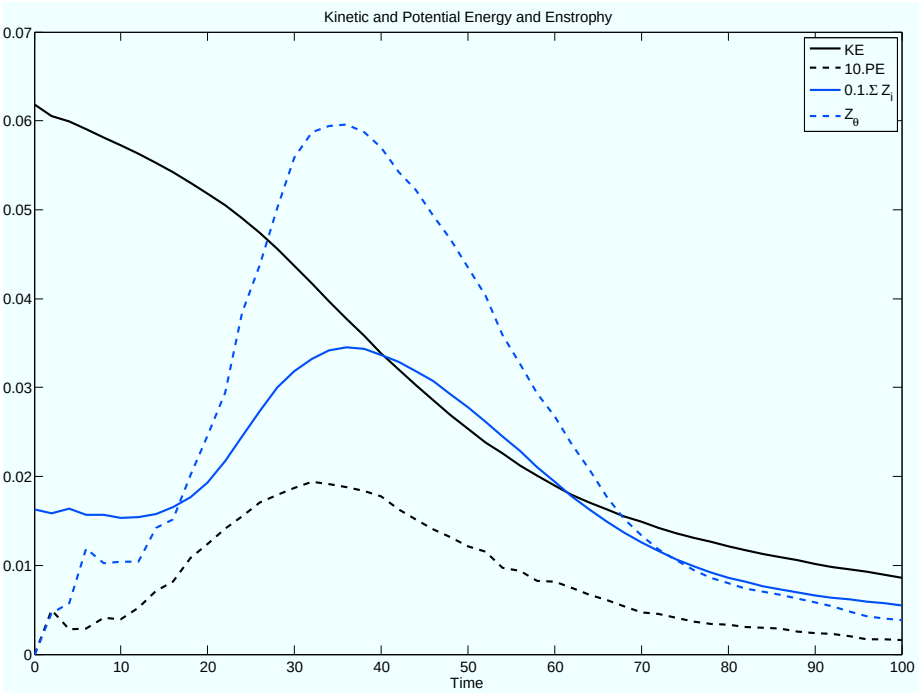

Figure 4.36: Evolution of total kinetic energy, total potential energy, scalar variance dissipation and sum total enstrophy against time.

A method through which the overall energy can dissipate is by energy moving from large scale structures to small scale structures which the, due to viscosity, dissipate their energy into the fluid. By considering the energies in Fourier space we are able to see if this transfer of energy, from large scales which correspond to low wavenumbers to small scales which correspond to high wavenumbers, holds true. Figure 4.37 shows the kinetic energy transfer spectra for various times in the

y direction, here $T(k)$ represents the change in energy at wavenumber k and k_y the wavenumber in the y direction. One obtains the (kinetic) energy transfer in Fourier space by taking the Fourier transform of the Boussinesq equation 2.4 and multiplying it by $\tilde{\boldsymbol{u}}(k)$, the Fourier transform of velocity, to obtain

$$\frac{1}{2}\frac{\partial}{\partial t}\tilde{\boldsymbol{u}}^2(k) = \tilde{\boldsymbol{u}}(k) \cdot \widetilde{\boldsymbol{u} \times \boldsymbol{\zeta}}(k) + \tilde{w}(k)\,\tilde{\theta}(k) - Re^{-1}k^2\tilde{\boldsymbol{u}}^2(k) \tag{4.7}$$

In the first frame of Fig. 4.37 we observe that at $t = 2$ and $t = 6$ kinetic energy is leaving low wavenumbers, $T(k) < 0$, and that some of this energy is deposited at larger wavenumbers e.g. at $t = 2$ $T(k) > 0$ between $k_y = 2.5$ and $k_y = 4$. The loss of kinetic energy at low wavenumbers and gain at high wavenumbers continues to be seen at later times, at $t = 8$ a marked amount of energy enters the wavenumbers between 1 and 2, some of this energy between wavenumbers 1 and 1.5 later leaves at $t = 24$. At late times, once enstrophy is rapidly dissipating, we observe that energy is essentially transferring out of all wavenumbers, that is, leaving the large scales into the small and rapidly dissipating into the fluid. Potential energy follows a similar method of dissipation, though initially energy must enter at the low wavenumbers for potential energy to initially grows from zero.

Figure 4.38 shows the potential energy transfer spectra in y for various time. On average, until $t = 32$ which is around the time potential energy begins to dissipate, we see that energy enters at the large scales. We know that the origin of this energy is from the kinetic energy since initially potential energy is zero and we also see no cascade of energy from the small scales to the large scales, which would manifest in $T(k) < 0$ at large wavenumbers.

From the figures of kinetic and potential energy transfer spectra we observe the general movement of energy from small wavenumbers to large wavenumbers and on to dissipation. As such we conclude that the zigzag instability provides for a method for the cascade of energy from the large scale structures to the small scale structures.

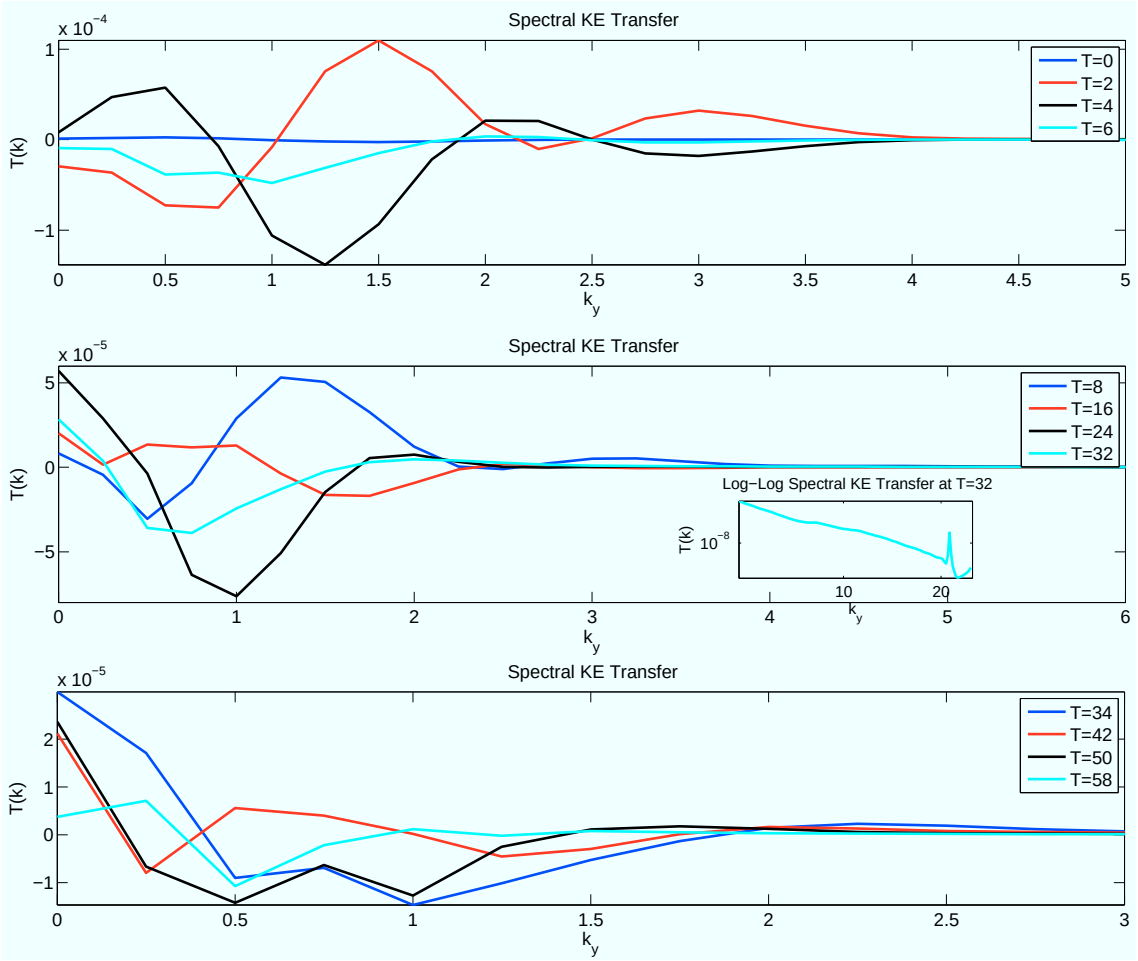

Figure 4.37: Spectral kinetic energy transfer against y wavenumber at various times.

Further to the transfer spectra of kinetic and potential energy, we consider also the spectra of kinetic and potential energies themselves. Figure 4.39 shows these spectra in the y direction against wavenumber. We observe that the kinetic and potential energy spectra quickly arrange such that they lay on to of each other, the cause for this is yet unstudied in this thesis and would be a subject for further work.

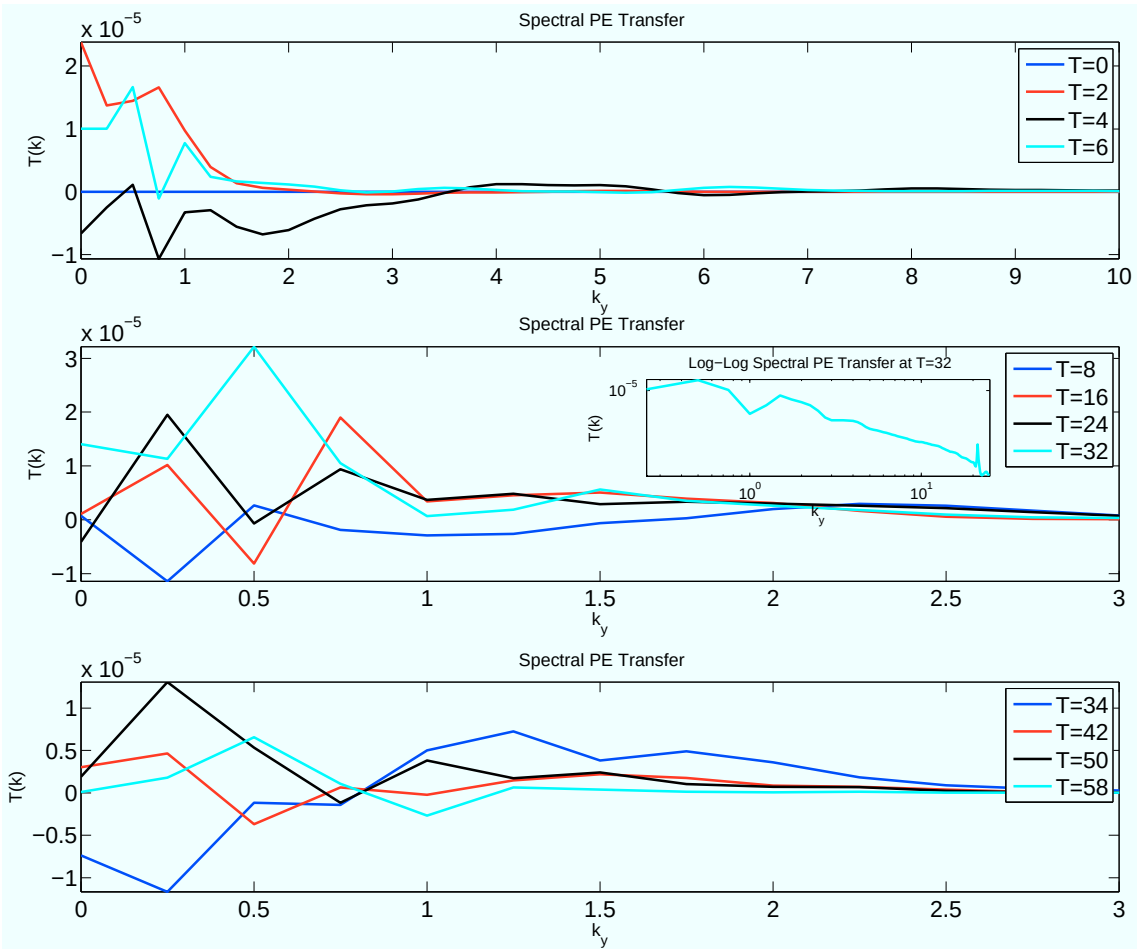

Figure 4.38: Spectral potential energy transfer against y wavenumber at various times.

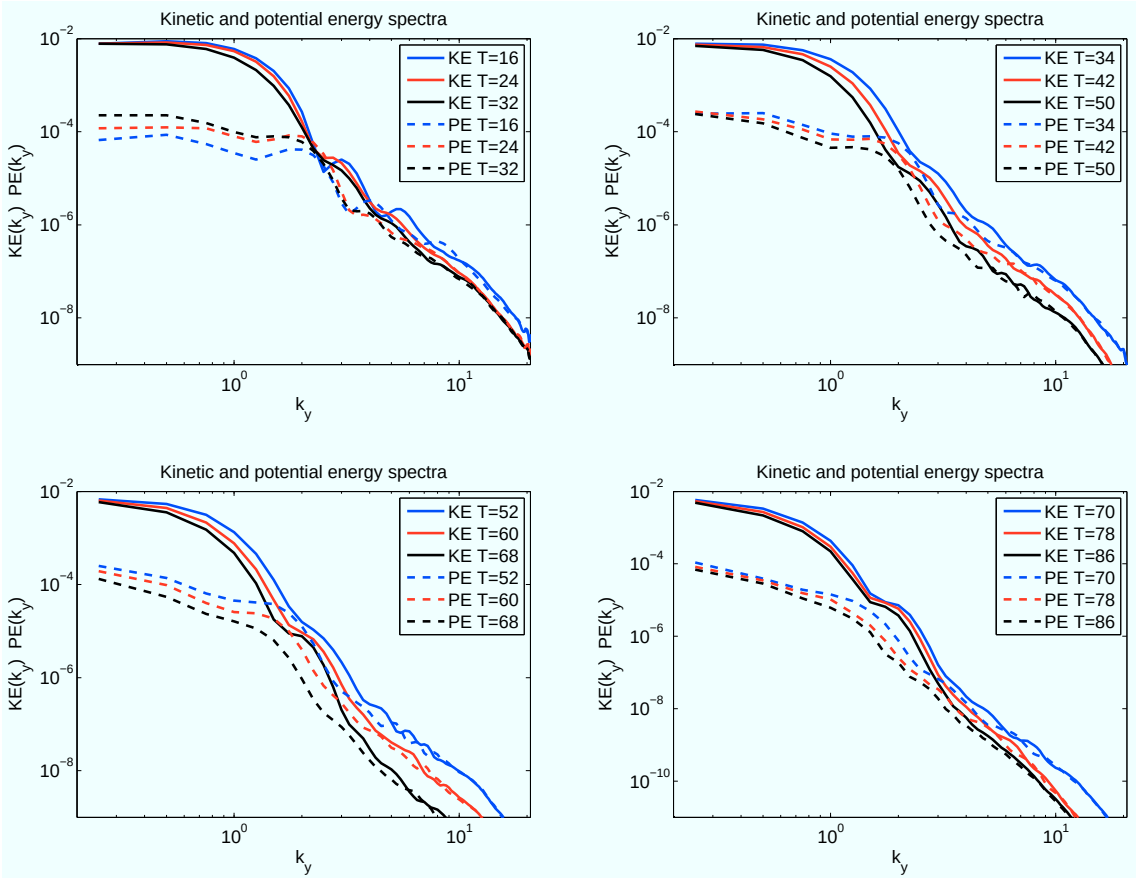

Figure 4.39: Kinetic and potential energy spectra against y wavenumber at various times.

4.6 Chapter Summary

In this chapter we began by introducing the idea of perturbing the vorticity of the vortex column rather than the velocity field as had previously been done. We showed that with this approach, symmetrically perturbing the vortex columns led to results similar to those performed by Deloncle et al. (2008, [3]), validating this new method of vortex initialisation. We discussed then, that this initial vortex profile, though evolving to produce a zigzag instability, achieved this at a much later time than had been observed in the experimental results of Billant and Chomaz (2000, [2]). In order to address this discrepancy we proposed alternate initial profiles that had the perturbations offset from one another and/or applied in a direction perpendicular to the direction of vortex column propagation. Our approach of perturbing the vortex column rather than the surrounding field allowed for this class of non-symmetric perturbations to be considered.

Of the four new initial profiles we considered in this chapter, we found that perturbations applied to the vortex columns that were offset from one another and in a direction parallel to vortex propagation lead to the fastest growth in enstrophy and development of the zigzag instability. We saw that this growth occurred approximately 40% quicker than the numerical calculations [3] and at a similar time to that seen in the experimental results [2]. We showed that the maximum growth rate of this initial profile excedes the expected maximum theoretical growth rate derived by Billant and Chomaz [24] and hence this new initial condition provides a faster route to the onset of the zigzag instability. We identified the mechanism by which this initial profile allowed for the rapid onset and growth of the zigzag instability, namely, the initial bending of the vorticies caused the gradient of the temperature scalar, θ, to grow large in the corners of these bends. This then caused a growth in the baroclinic production of enstrophy which pulled and stretched these bends of the vortex columns increasingly flattening them. This flattening further increased the

scalar gradient and thus closing the feedback loop causing the instability to grow. Growth stops only when the vortex sheets have flattened sufficiently for viscous effects to dominate and dissipate the energy away into the fluid. We noted that in flattening and stretching of the vortex bends, the vortex stretching terms acted primarily in the y direction and the baroclinic production terms in the x direction.

In the final part of this chapter, we provided evidence for the existence of a forward energy cascade, from the large scales to small scales. We showed that at early times, energy is transferring out of the low wavenumbers and at later times, energy is entering in at the higher wavenumbers. We suggest that since the zigzag instability provides a pathway for energy to dissipate from large scales to small scales, then it should be considered carefully when forecasting using any advection scheme that may smooth out any small scale structures that have the potential to develop into an instability.

Chapter 5

Conclusion

Our aims in this thesis were to present a new approach to initialising a pair of counter rotating vortices, in a strongly stratified fluid, which would become unstable to the zigzag instability much faster than any prior DNS. Secondly, we aimed to show that the zigzag instability provided a mechanism for energy to transfer from large scales to small scales through both kinetic and potential energy.

We began in Chapter 1 by introducing some theory on the energy cascade in turbulent fluids based on dimensional arguments and noted that this energy cascade of $k^{-5/3}$ in the mesoscales of the atmosphere has been observed both experimentally, by aircraft measurements, and numerically, through DNS. We raised the question as to whether the cascade is a backward one, as expected by 2D dynamics, or a forward one, as expected in 3D dynamics. We summarised the arguments that suggest that the energy cascade is indeed a forward one, from low wavenumbers to high. This however raised a further question as to how the mesoscale dynamics behave since the physical dimensions of the mesoscale are not consistent with fully 3D turbulent motions however the direction of the energy cascade is not consistent with 2D turbulent dynamics. We suggest that the zigzag instability observed in strongly stratified fluids provides a route for energy to dissipate away at the small scales.

In Chapter 2, we introduced the standard equations used to simulate the motions of geophysical fluids based on the Boussinesq approximation of the incompressible Navier-Stokes equations. We derived the vorticity formulation of these equations which are the set of equations we simulate in Chapter 4. We also derive the enstrophy formulation which allows us to identify the terms that contribute to growth in enstrophy, vortex stretching and Baroclinic vorticity production.

We described previous numerical and experimental work on the zigzag instability in Chapter 3, and described the advantages of a new alternate form of an initial perturbation based on vorticity perturbation rather than velocity perturbation. This allows us to perturb vortex columns more locally and also independently of each other giving us the option of offsetting the perturbation of the columns from each other in the vertical direction. The main results of the thesis were presented in Chapter 4. We began by confirming our method of perturbing the vortex columns was consistent with prior DNS by Deloncle et al. (2008). We showed visually similar results and similar evolutions of total enstrophy (a measure of the growth rate of the zigzag instability) at similar time scales. We then proposed initial profiles of vortex columns that maybe a more physically realistic scenario. These profiles all had perturbations locally applied, that is the spread of the perturbation was approximately a third of the column, but varied in direction and vertical displacement.

We measured the total enstrophy for each of these initial profiles, as well as their components in the x, y and z directions, and found that the profile that became unstable to the zigzag instability the quickest was the initial profile with perturbations that were offset from one another and acted in a direction parallel to the propagation of the vortex columns. This profile reaches peak enstrophy 40% quicker than the DNS of Deloncle et al. and occurs at a similar time to the experimental results in [2]. This profile reached a peak after approximately 39 seconds $\left(36 \times \frac{2\pi r^2}{\Gamma}\right)$ with the experimental results reaching the corresponding peak 35 seconds after the flaps had closed and reopened [2]. We took this profile found to be most unstable

and studied the growth in enstrophy in further detail, considering its components of vortex stretching and Baroclinic production. We found that enstrophy production is dominated by the vortex stretching term over Baroclinic production and further that vortex stretching occurs in the direction perpendicular to the propagation of the vortices, that is occurs in the y direction, and Baroclinic production occurs mainly in the x direction, the direction of vortex propagation.

We then considered the kinetic and potential energies of the system. We found that the kinetic energy is at a peak at the start of the simulation and decays from this peak, however potential energy is initially zero and grows to a peak value which is reached a few timesteps prior to the peak in enstrophy, after which it too decays. We finally showed evidence of both potential and kinetic energy transferring out of the low wavenumbers (the large scales) and entering into the high wavenumbers, evidence for a forward energy cascade.

We have described a mechanism that provides a potential route for energy to dissipate within a fluid from large scale structures to the small scales. Identifying this mechanism, however, relies upon one accurately resolving and tracking a perturbation which, relative to its surrounding vorticity, maybe small. Given this inherent problem of structure size along with the requirement that a weather forecast model provides results within an useful time frame, resulting in the smoothing out of the smaller scale structures, could provide a partial explanation for the lack of the $k^{-5/3}$ energy spectrum that is observed in the atmosphere experimentally but not identified in numerical weather forecasting models.

5.1 Further Work

In §4.5.3 we observed the transfer of kinetic energy out of low wavenumbers and potential energy into low wavenumber, the theory that the initial gain in potential energy at low wavenumbers, though logical, should be studied quantitatively. One

would hope to better understand how much of the energy transfers out of the kinetic and then directly into the potential energy.

We noted in Fig. 4.39 that the spectra of kinetic and potential energy, after a certain wavenumber, lie on top of each other. This behaviour is somewhat unusual though a suggested explanation for this could be related to internal waves. It is possible that at some point both the kinetic and potential energies become trapped in internal waves of the same frequency from which they are unable to escape.

A third aspect requiring additional study has been noted by Augier et al. [27], in which after the zigzag instability has formed and developed, a further instability of Kevin-Helmholtz type can develop at late times. This secondary instability could provide a further method for energy to cascade into the small scales. In order to study this, a calculation of greater resolution and Reynolds number would be required. Currently, a calculation of mesh grid $256 \times 512 \times 512$ is running and given more time and computational resources to analyse the results I would hope to verify this results and understand its implication on the cascade of kinetic and potential energy.

Bibliography

[1] G. Nastrom and K. Gage, "A climatology of atmospheric wavenumber spectra of wind and temperature observed by commercial aircraft," *J. Atmos. Sci.*, vol. 42, no. 9, pp. 950–960, 1985.

[2] P. Billant and J.-M. Chomaz, "Experimental evidence for a new instability of a vertical columnar vortex pair in a strongly stratified fluid," *J. Fluid Mech.*, vol. 418, pp. 167–188, 2000.

[3] A. Deloncle, P. Billant, and J.-M. Chomaz, "Nonlinear evolution of the zigzag instability in stratified fluids: a shortcut on the route to dissipation," *J. Fluid Mech.*, vol. 599, pp. 229–239, 2008.

[4] M. Lesieur, *Turbulence in Fluids*. Springer, 1997.

[5] U. Frisch, *Turbulence: The Legacy of A. N. Kolmogorov*. Cambridge University Press, 1995.

[6] J. Cho and E. Lindborg, "Horizontal velocity structure functions in the upper troposphere and lower stratosphere: 1. observations," *J. Geophys. Res.*, vol. 106, no. 10, pp. 223–232, 2001.

[7] P. Constantin and C. Fefferman, "Scaling exponents in fluid turbulence: some analytic results," *Nonlinearity*, vol. 7, no. 1, pp. 41–57, 1994.

[8] E. Lindborg, "The energy cascade in a strongly stratified fluid," *J. Fluid Mech.*, vol. 550, pp. 207–242, 2006.

[9] J. Riley and S. deBruynKops, "Dynamics of turbulence strongly influenced by buoyancy," *Phys. Fluids*, vol. 15, no. 7, pp. 2047–2059, 2003.

[10] K. Tung and W. Orlando, "The k^{-3} and $k^{-5/3}$ energy spectrum of atmospheric turbulence: Quasigeostrophic two-level model simulation," *J. Atmos. Sci.*, vol. 60, pp. 824–835, 2003.

[11] P. Billant and J.-M. Chomaz, "Theoretical analysis of the zigzag instability of a vertical columnar vortex pair in a strongly stratified fluid," *J. Fluid Mech.*, vol. 419, pp. 29–63, 2000.

[12] P. Billant and J.-M. Chomaz, "Three-dimensional stability of a vertical columnar vortex pair in a stratified fluid," *J. Fluid Mech.*, vol. 419, pp. 65–91, 2000.

[13] G. Shutts, "A kinetic energy backscatter algorithm for use in ensemble prediction systems," *Q. J. R. Meteorol. Soc.*, vol. 131, pp. 3079–3102, 2005.

[14] J. McWilliams, *Fundamentals of Geophysical Fluid Dynamics*. Cambridge University Press, 2006.

[15] J.-T. Lin and Y.-H. Pao, "Wakes in stratified fluids," *Ann. Rev. Fluid. Mech.*, vol. 11, pp. 317–338, 1979.

[16] Y. Kimura and J. Herring, "Diffusion in stably stratified turbulence," *J. Fluid Mech.*, vol. 328, pp. 253–269, 1996.

[17] J. Herring and O. Métais, "Numerical experiments in forced stably stratified turbulence," *J. Fluid Mech.*, vol. 202, pp. 97–115, 1989.

[18] A. Fincham, T. Maxworthy, and G. Spedding, "Energy dissipation and vortex structure in freely decaying stratified grid turbulence," *Dyn. Atmos. Oceans*, vol. 23, pp. 155–169, 1996.

[19] C. Williamson and J.-M. Chomaz, "The exploding vortex pair," *Phys*, vol. 9, p. S4, 1997.

[20] P. Otheguy, J.-M. Chomaz, and P. Billant, "Elliptic and zigzag instabilities on co-rotating vertical vortices in a stratified fluid," *J. Fluid Mech.*, vol. 553, pp. 253–272, 2006.

[21] P. Otheguy, P. Billant, and J.-M. Chomaz, "Theoretical analysis of the zigzag instability of a vertical co-rotating vortex pair in a strongly stratified fluid," *J. Fluid Mech.*, vol. 584, pp. 103–123, 2007.

[22] P. Billant, "Zigzag instability of vortex pairs in stratified and rotating fluids. part 1. general stability equations," *J. Fluid Mech.*, vol. 660, pp. 354–395, 2010.

[23] P. Otheguy, P. Billant, and J.-M. Chomaz, "The effect of planetary rotation on the zigzag instability of co-rotating vortices in a stratified fluid," *J. Fluid Mech.*, vol. 553, pp. 273–281, 2006.

[24] P. Billant, A. Deloncle, J.-M. Chomaz, and P. Otheguy, "Zigzag instability of vortex pairs in stratified and rotating fluids. part 2. analytical and numerical analyses," *J. Fluid Mech.*, vol. 660, pp. 396–429, 2010.

[25] R. Kerr, "Higher order derivative correlations and the alignment of small-scale structures in isotropic numerical turbulence," *J. Fluid Mech.*, vol. 153, pp. 31–58, 1985.

[26] P. Constantin, "Geometric statistics in turbulence," *SIAM Rev.*, vol. 36, no. 1, pp. 73–98, 1994.

[27] P. Augier and P. Billant, "Onset of secondary instabilities on the zigzag instability in stratified fluids," *J. Fluid Mech.*, vol. 682, pp. 120–131, 2011.

[28] M. Brend and P. Thomas, "Decay of vortex rings in a rotating fluid," *Phys. Fluids*, vol. 21, no. 4, 2009.

[29] C. Cao and E. Titi, "Global well-posedness of the three-dimensional viscous primitive equations of large scale ocean and atmosphere dynamics," *Annals Math.*, vol. 166, pp. 245–267, 2007.

[30] H. Chen, J. Herring, R. Kerr, and R. Kraichnan, "Non-gaussian statistics in isotropic turbulence," *Phys. Fluids A*, vol. 1, no. 11, pp. 1844–1854, 1989.

[31] P. Davidson, P. Staplehurst, and S. Dalziel, "On the evolution of eddies in a rapidly rotating system," *J. Fluid Mech.*, vol. 557, pp. 135–144, 2006.

[32] D. Dritschel, M. de la Torre Juárez, and M. Ambaum, "The three-dimensional vortical nature of atmospheric and oceanic turbulent flows," *Phys. Fluids*, vol. 11, no. 6, pp. 1512–1520, 1999.

[33] K. Hamilton, "High resolution global modeling of the atmospheric circulation," *Adv. Atmos. Sci.*, vol. 23, no. 6, pp. 842–856, 2006.

[34] R. Kerr, "Vortex stretching as a mechanism for quantum kinetic energy decay," *PRL*, vol. 106, no. 22, 2011.

[35] R. Kerr, "Evidence for a singularity of the three-dimensional incompressible euler equations," *Phys. Fluids A*, vol. 5, no. 7, pp. 1725–1746, 1993.

[36] R. Kerr and F. Hussain, "Simulation of vortex reconnection," *Physica D*, vol. 37, pp. 474–484, 1989.

[37] R. Kerr and G. King, "Evidence for a mid-latitude, mesoscale downscale energy cascade from the marine boundary layer," *J. Atmos. Sci.*, 2009.

[38] E. Lindborg, "The effect of rotation on the mesoscale energy cascade in the free atmosphere," *Geophys. Res. Lett.*, vol. 32, 2005.

[39] E. Lindborg and J. Cho, "Horizontal velocity structure functions in the upper

troposphere and lower stratosphere: 2. theoretical considerations," *J. Geophys. Res.*, vol. 106, no. 10, pp. 233–241, 2001.

[40] T. Miyazaki and Y. Fukumoto, "Three-dimensional instability of strained vortices in a stably stratified fluid," *Phys. Fluids A*, vol. 4, no. 11, pp. 2515–2522, 1992.

[41] J. Riley and M.-P. Lelong, "Fluid motions in the presence of strong stable stratification," *Ann. Rev. Fluid. Mech.*, vol. 32, pp. 613–657, 2000.

[42] P. Staplehurst, P. Davidson, and S. Dalziel, "Structure formation in homogeneous freely decaying rotating turbulence," *J. Fluid Mech.*, vol. 598, pp. 81–105, 2008.

[43] M. Waite, "Stratified turbulence at the buoyancy scale," *Phys. Fluids*, vol. 23, no. 6, 2011.

[44] M. Waite and P. Smolarkiewicz, "Instability and breakdown of a vertical vortex pair in a strongly stratified fluid," *J. Fluid Mech.*, vol. 606, pp. 239–273, 2008.